University of Mississippi

eGrove

Electronic Theses and Dissertations | Graduate School

2014

The Effects Of Diffusion, Capillary Heterogeneity, And Porous Media Morphology On CO2 Migration In Porous Media

Oluseye Babafemi Adeyemi
University of Mississippi

Follow this and additional works at: https://egrove.olemiss.edu/etd

 Part of the Chemical Engineering Commons

Recommended Citation

Adeyemi, Oluseye Babafemi, "The Effects Of Diffusion, Capillary Heterogeneity, And Porous Media Morphology On CO2 Migration In Porous Media" (2014). *Electronic Theses and Dissertations*. 401.
https://egrove.olemiss.edu/etd/401

This Dissertation is brought to you for free and open access by the Graduate School at eGrove. It has been accepted for inclusion in Electronic Theses and Dissertations by an authorized administrator of eGrove. For more information, please contact egrove@olemiss.edu.

THE EFFECTS OF DIFFUSION, CAPILLARY HETEROGENEITY, AND POROUS MEDIA MORPHOLOGY ON CO_2 MIGRATION IN POROUS MEDIA

A Thesis
presented in partial fulfilment of requirements for the degree of

Master of Science

Department of Chemical Engineering
The University of Mississippi

OLUSEYE B. ADEYEMI

DECEMBER 2014

Copyright© by Oluseye B. Adeyemi 2014
ALL RIGHTS RESERVED

ABSTRACT

The Modified Invasion Percolation (MIP) model was used to simulate the invasion of CO_2 into a medium initially saturated with water and the style of capillary heterogeneity in combination with buoyancy and viscous forces were varied to yield 105 different simulation scenarios. Thereafter, the invasion of the CO_2 gas is simulated using a finite difference model and the effective mass transfer coefficient is determined and linked to various styles of capillary heterogeneity

Results show that an increase in saturation does not result in an increase in mass transfer coefficient rather, the surface area, which in turn is controlled by the interplay of capillary heterogeneity effects and buoyancy forces, control the average mass transfer coefficient and the fractional mass left. We further correlated the mass transfer coefficient with the average surface area and saturation and we found that a very strong positive correlation coefficient exists between the surface area of the CO_2 and mass transfer coefficient and a weak negative correlation coefficient exists between the average mass transfer coefficient and saturation exists, which improves with increasing stratification and increasing buoyancy forces.

We also used a harmonic mean model to estimate the effective diffusivity in a Room Temperature Ionic Liquid (RTIL) membrane. A metallic porous membrane was thoroughly saturated with Emim(Tf_2N) and placed in a diffusion chamber. CO_2 gas was injected into the upper diffusion chamber and was allowed to completely diffuse through the RTIL into the lower diffusion chamber. Lag-time technique was used to analyze the pressure-time data. Two different

membrane configurations were used; 0.2-0.2μ and 0.5-0.5μ. Results show that the harmonic mean model reasonably predicts the effective diffusivity obtained from the experimental measurements.

ACKNOWLEDGMENTS

I would like to say a very big thank you to my advisors; Dr Paul Scovazzo and Dr Robert Holt for their guidance, understanding and patience. I am forever indebted. Special thanks to Dr Peter Sukanek for his inputs into this thesis as well. I am really grateful. I would also like to thank the entire Chemical Engineering faculty, particularly Dr Clint Williford – thanks for providing the funds and the knowledge you have imparted.

My sincere appreciation goes to my family for their unrelenting and unflinching support for me throughout the entire period. My heartfelt gratitude also goes to Wasiu Omotoso and Anuoluwapo Akintude; thanks for the motivation and encouragement. To my colleagues in the Chemical Engineering department; Olugbenga Ojo, Poh Lee Cheah, Chris Riley, thanks for the memories we made together.

TABLE OF CONTENTS

LIST OF FIGURES

LIST OF TABLES

CHAPTER 1

THE EFFECTS OF DIFFUSION, CAPILLARY HETEROGENEITY, AND POROUS MEDIA MORPHOLOGY ON CO_2 MIGRATION IN POROUS MEDIA

1.1 INTRODUCTION

This thesis explores the effects of diffusion, capillary heterogeneity and porous media morphology on CO_2 migration in porous media. Chapter 1 gives a broad overview into the organization of the thesis.

Chapter 2 explores the influence of diffusion and capillary heterogeneity effects on CO_2 leakage from a borehole. This was done by modeling the mass transfer coefficient, fractional mass left, average surface area and the average saturation for a number of scenarios using modified invasion percolation and solving the diffusion equation using numerical methods. The chapter has a short introduction, the methods, results, a summary and discussion page that ties the preceding sections together.

Chapter 3 examines the influence of porous support morphology on mass transport in Room Temperature Ionic Liquid (RTIL) membranes. The effective diffusivity of CO_2 through RTIL membranes was determined experimentally by passing CO_2 through a RTIL membrane in a diffusion chamber and using a lag time technique to evaluate the pressure-time relationship. The chapter comprises of a short introduction, literature review, details of the experimental procedure, and relevant results.

Chapter 4 includes a summary and discussion of the important results obtained from the previous two chapters.

CHAPTER 2

CAPILLARY HETEROGENEITY EFFECTS ON CO_2 DIFFUSION FROM A WELL LEAKAGE

2.1 INTRODUCTION

While there are many alternatives for reducing the quantities of carbon dioxide in the earth's atmosphere, Carbon Capture and Sequestration (CCS) continues to be one of the most attractive (Holloway, 2007). CCS involves the separation of CO_2 from industrial emissions and its consequent injection in gas phase into suitable deep geological systems. These systems include saline formations, depleted oil and gas fields and un-mineable coal systems.(Edlmann, Haszeldine, & McDermott, 2013; Elena, 2011).

A number of potential leakage pathways have been identified, including: the diffusive loss through the seals (i.e. the cap-rock), leakage through pore spaces when capillary breakthrough pressure has been exceeded, leakage through faults and fractures, and leakage as a result of poorly abandoned and degraded wells. A combination of these leakage pathways is also possible. Although the leakages may be small initially, they could result in disastrous consequences over a long period of time – either in the form of contamination of potable water in the aquifer due to brine displacement or through the escape of CO_2 back into the atmosphere (Dobossy, Celia, & Nordbotten, 2011; Song & Zhang, 2013).

For most potential leakage pathways, molecular diffusion will be the dominant transport mechanism and might even deplete the formation of CO_2 by either transporting it to the atmosphere or to a shallow aquifer if reactions between CO_2 and rock minerals are neglected (Šimůnek & Suarez, 1993). The spatial distribution of CO_2 fluxes has been modeled by a number of researchers mostly by statistical correlation with parameters. The influence of air temperature, soil temperature and soil water content have been evaluated on the CO_2 concentration in the soil over several years (Buyanovsky & Wagner, 1983), the average CO_2 concentrations in soil have also been predicted by evapotranspiration using regression analysis (Brook, Folkoff, & Box, 1983; Kiefer, 1990).

The most rapid transport pathway for CO_2 to the environment is likely along poorly constructed or old and degraded boreholes. Access to the subsurface for CCS requires the use of injection boreholes and many geological systems are penetrated by existing boreholes. These boreholes provide a potential migration pathway for sequestered CO_2 to the environment (Burnside, Shipton, Dockrill, & Ellam, 2013; Lewicki, Birkholzer, & Tsang, 2006).

This thesis continues the research on the broad factors affecting CO_2 leakage in a well bore. We examine the effective mass transfer coefficient of a CO_2 plume in shallow aquifer resulting from a well bore leak, subject to capillary, viscous and buoyancy forces. The displacement of the denser wetting phase (i.e. water by the lighter CO_2 gas) was simulated using a quasi-3D, Modified Invasion Percolation (MIP) model that include capillary forces, buoyancy forces, and a first order approximation of viscous forces. Following invasion, the diffusion of the CO_2 gas into and through the aqueous phase is simulated using a block-centered finite difference model, and the effective mass-transfer coefficient is determined and linked to various styles of capillary heterogeneity.

We used the approach of Roecker (2012) and systematically varied the style of capillary heterogeneity from unstructured to 'stratified' to mimic the range of capillary heterogeneity found in nature. Additionally, the strength of buoyancy and viscous forces are also varied, and the average fractional mass left in the domain and effective mass transfer coefficient is calculated and correlated with the surface area and saturation of the invaded CO_2. All the percolation simulations are non-dimensional and are scaled using the gas entry pressure of a porous medium. Over 1000 simulations were carried out to quantify the influence of and uncertainty due to variations in capillary heterogeneity, buoyancy forces and viscous forces on CO_2 surface area and saturation. The capillary heterogeneity was systematically varied to reflect the common heterogeneity found in natural systems

2.2 METHODS

2. 2.1 Modified Invasion Percolation Model

We proceed in the same manner as in (Roecker, 2012) by using an MIP approach to simulate the invasion of CO_2 into a medium initially saturated with water under the combined influence of capillary, buoyancy and viscous forces. A distinction is made between Invasion Percolation (Wilkinson & Willemsen, 1983) and MIP by defining a macro near pore scale block defined and characterized by a local threshold spanning pressure that represents the behavior of the subscale network (Holt, 2003). We discretize the domain into an array of grid blocks and an invasion pressure is defined based on the difference between the invading and defending phases;

$$P_I^* = P_S^* + \Delta\rho g Z^* + (\Delta \mathrm{P}_v^*) \tag{2.1}$$

Where P_S^* is the capillary spanning pressure ($ML^{-1}T^1$), $\Delta\rho = \rho_{defender} - \rho_{invader}$ is the difference in densities of the defending phase and invading phase (ML^3), g is the acceleration due to gravity in the Z-direction (LT^2), Z^* is the coordinate in the Z direction (L) and $\Delta \mathrm{P}_v^*$ is the difference in viscous pressure between the defending and invading phase ($ML^{-1}T^{-1}$). The dimensionless invasion pressure is obtained by dividing equation (1) by the average spanning pressure $< P_S^* >$;

$$P_I = \frac{P_S^*}{\left\langle P_S^* \right\rangle} + B_o Z + \frac{\left(\mathrm{P}_v^{\,d} - \mathrm{P}_v^{\,i}\right)}{\left\langle P_S^* \right\rangle}$$

(2.2)

The dimensionless Bond Number is defined as

$$B_o = \frac{\Delta\rho g \Delta Z^*}{\left\langle P_S^* \right\rangle} \tag{2.3}$$

ΔZ^* is the grid block length in the Z-direction (L). The dimensionless Z-coordinate is defined as

$$Z = \frac{Z^*}{\Delta Z^*} \tag{2.4}$$

The Bond Number reflects the strength of the buoyancy forces. For the simulations here, the Bond Number was varied between 0, 0.1 and 1 to represent different strength of the buoyancy forces.

The viscous pressure in the defending fluid was set to zero for all simulations, to simulate static, non-flowing groundwater conditions. For the invading fluid, the viscous pressure is calculated by a first order approximation for steady flow from a point source in spherical coordinates with the reduced equation being

$$\frac{P_v^{i*}}{\left\langle P_S^* \right\rangle} = VSN\left(\frac{1}{r} - \frac{1}{R}\right) \tag{2.5}$$

Where VSN is the dimensionless viscous scaling number, r is the dimensionless grid-block radial coordinate (-), and R is the dimensionless radius of influence (-). An R value of 1000 was kept constant for all simulations. We selected VSN values of 0 and 250; a VSN value of 250 is equivalent to a CO_2 volumetric discharge rate of $0.03 m^3/d$ in a typical sandstone and 3×10^{-4} m^3/d in a typical mudrock or shale.

An FFT approach was used to generate correlated spanning-pressure fields. A two-dimensional, correlated random field (512 X 512) with a standard normal distribution is generated, the value at each nodal location is mapped to an associated probability, and finally the nodal spanning pressure is determined from the nodal probability (P) using the van Genuchten (1980) pressure saturation model

$$P_S = \frac{1}{\alpha}\left\{\left[\left(\frac{1}{P}\right)^{\frac{1}{1-\frac{1}{N}}}\right]-1\right\}^{\frac{1}{N}} \tag{2.6}$$

Where P_S is the spanning pressure, α is a model parameter related to the air-entry pressure, N is a model parameter associated with the pore-size distribution. Alpha (α) values of 1 and N values of 1.5 were kept constant for all simulations. The style of capillary heterogeneity in each field is defined by a fixed correlation ratio – the ratio of the horizontal to vertical correlation lengths. Correlation ratios of 1, 10, 20, 50, and 100 were used to reflect increasing horizontal stratifications. Values of 1, 10, and 50 are used as the dimensionless vertical correlation lengths. The horizontal correlation lengths are varied to maintain the aforementioned specified correlation ratios. Figure 2.1 shows some spanning pressure fields corresponding to a correlation ratio of 1, 20 and 100.

The MIP algorithm sorts all blocks based on P_I and invades the block with the lowest invasion pressure. The non-wetting phase invasion proceeds from a source on the left edge of the domain towards the top or right edge of the boundary. A network connectivity of 8 (communication is allowed with all surrounding blocks) to approximate three-dimensional behavior within a two-dimensional network. The process continues until the blocks along the active interface reach the top or right edge boundaries, the percolation threshold.

The percolation model simulates leakage from a point source and a line source along the left edge of the domain. The model defines an initial wetted surface of CO_2 that acts as the leak source. The wetted surface is defined as all the possible nodes that are in contact with the growing cluster. The initial wetted surface for a point source allows invasion of CO_2 only into the bottom-most node on the left-hand side of the domain. For the larger leak source, the bottom 102 nodes along the left hand side of the domain are considered invadable at the start of the simulation. After the invasion process, we coupled the output of the invasion model to the diffusion model. Table 2.1 shows the summary values for all the simulation values

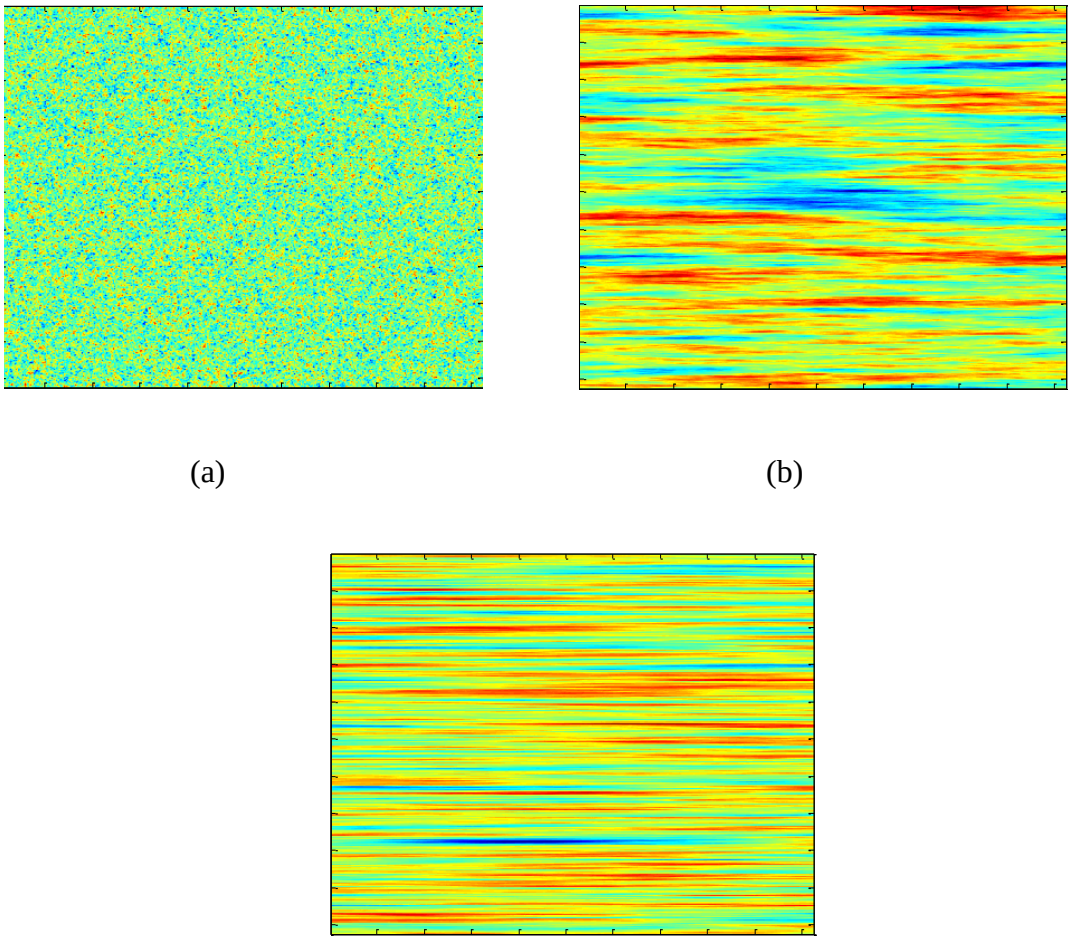

Figure 2.1: Typical spanning pressure fields
(a) a vertical correlation length of 1 and correlation ratio of 1 (b) vertical correlation length of 10 and a correlation ratio of 20 (c) vertical correlation length of 50 with a correlation ratio of 100. The horizontal correlation length will vary to maintain the specified correlation ratio

2. 2.2 The Diffusion Equation

The change in concentration of a diffusing gas due to concentration gradient is modeled by numerically solving the diffusion equation. It is a parabolic equation derived from the fundamental laws describing the flux of concentration using the law of conservation of mass. The three-dimensional diffusion equation is given as;

$$\nabla^2 C = \frac{dC}{dt} \tag{2.7}$$

Equation (2.7) is the non-dimensional form of the diffusion equation. The non-dimensional form was obtained by introducing a new positional variable L (L) and a new time variable defined as

$t = \frac{t^* D}{L^2}$ where t* is the dimensional form of time (T) and D is the diffusion coefficient (L^2T^{-1})

For the simulations, a 2D approximation of the diffusion equation was used; when written out using finite difference approximations, the equation becomes

$$\begin{aligned}(\Delta x_i \Delta z_i)\frac{C_{i,j}{}^{n} - C_{i,j}}{t_n - t_{n-1}} = &\left(\frac{1}{\Delta x}\right)_{i+\frac{1}{2},j}\left(C_{i+1,j}{}^{n} - C_{i,j}{}^{n}\right)\Delta z_j + \left(\frac{1}{\Delta x}\right)_{i-\frac{1}{2},j}\left(C_{i-1,j}{}^{n} - C_{i,j}{}^{n}\right)\Delta z_j \\ &+\left(\frac{1}{\Delta z}\right)_{i,j+\frac{1}{2}}\left(C_{i,j+1}{}^{n} - C_{i,j}{}^{n}\right)\Delta x_i + \left(\frac{1}{\Delta z}\right)_{i,j-\frac{1}{2}}\left(C_{i,j-1}{}^{n} - C_{i,j}{}^{n}\right)\Delta x_i \end{aligned} \tag{2.8}$$

where i, j are subscripts indicating node location, n is a subscript indicating the time step, C (x, z, t) is the concentration of the diffusing gas, t is the time, Δx – is the length of the finite-difference cell in the x-direction; and Δz – is the length of the finite difference cell in the z-direction,.

The diffusion model was solved by representing the domain using a block-centered grid. The size of the MIP model domain was 512 X 512. For the diffusion process, we added an extra buffer of 100 blocks on either side to make a 712 X 712 blocks to move the effects of the boundaries away from the CO_2 invaded area. .The time step (dt) used was 0.0001 and the

equation was solved over 500 time steps. We assumed the diffusion coefficient remained constant across the domain. The spatial derivatives in two dimensions were approximated by the five-point, finite-difference, linear operator written for each node. To verify our numerical model, we solved the numerical model for a rectangular domain and compared with analytical solutions for simple cases of molecular diffusion subject to the following initial and boundary conditions

$C(x, z, 0) = 1.0$

$C = 0.0$ for $x = \pm 1$

$C = 0.0$ for $z = \pm 1$

The dimensionless length of the domain was 2 X 2 and was spaced uniformly at 0.00280899 in the x and z directions. The time step size was 0.0001 and was kept constant throughout the simulation period. The analytical and numerical solutions were virtually identical as shown in Figure 2.2.

The analytical solution was given by (Carslaw & Jaeger, 1986) as

$$\phi(x, z, t) = \frac{16}{\pi^2}\left(\sum_{i=0}^{\infty}\frac{(-1)^i}{2i+1}e^{\frac{-k(2i+1)^2\pi^2 t}{4}}\cos\frac{(2i+1)\pi x}{2}\right) \left(\sum_{i=0}^{\infty}\frac{(-1)^i}{2i+1}e^{\frac{-k(2i+1)^2\pi^2 t}{4}}\cos\frac{(2i+1)\pi z}{2}\right) \quad (9)$$

Furthermore, since the principle of conservation of mass requires that the net flux i.e. the cumulative sums of mass inflows and outflows must equal the accumulation of mass.

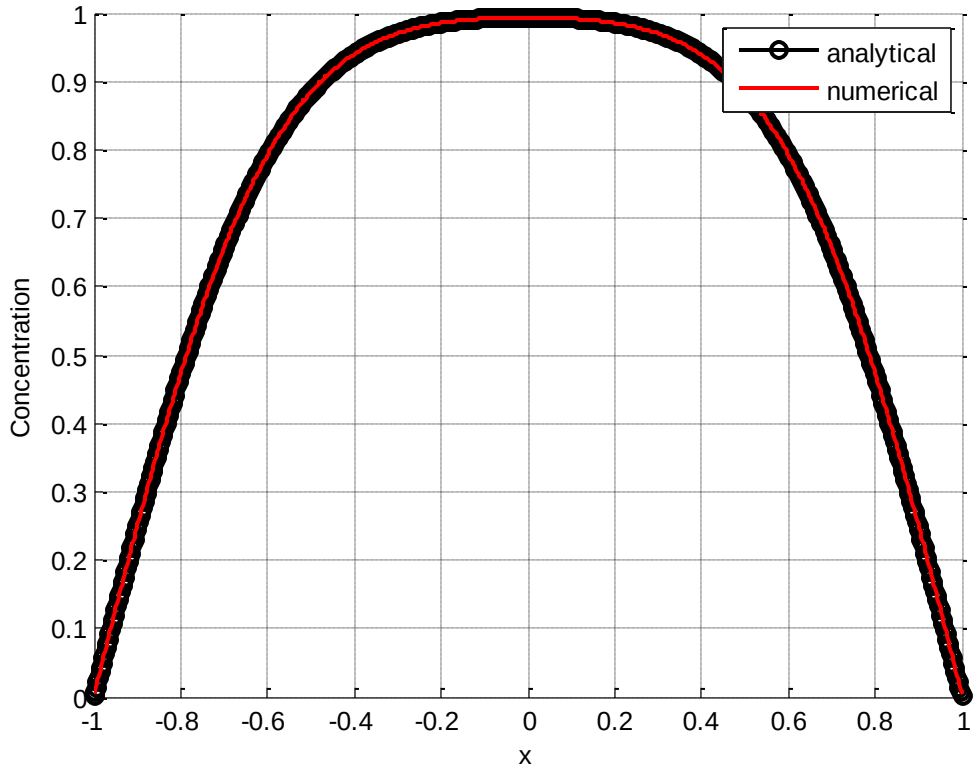

Figure 2.2: A comparison of the analytical and numerical solution for concentration distribution in a square domain at z = 0.9831.

Mass balance calculations were performed to help check the numerical accuracy and precision of the solution after each time step (Konikow & Bredehoeft, 1978). The mass balance was computed using

$$E_s = \frac{100.0\left(M_f - \Delta M_s\right)}{M_o - M_f}$$

Where M_f is the net mass flux (M), ΔM_s – change in mass stored in the domain (M), M_o is the initial mass of the solute (M)

The value of E_s after the end of 500 time steps was well below 1% which confirms the accuracy of our diffusion model. The invaded CO_2 cells were assumed to have a unit initial concentration and the gas was allowed to diffuse across the entire domain.

We employed a first order approximation for the rate of mass transfer into diffusive zones by defining by defining the change in concentration in our invaded nodes as

$$\frac{\partial C^*}{\partial t^*} = \alpha^* \left(C - C_n^*\right)$$

Where α^*[1/T] is the mass-transfer coefficient for diffusion; this approach enabled us to lump all the physical aspects of the diffusion process into a single parameter; C is the concentration in the invaded nodes and C_n^* represents the volumetric average concentration in the non-invaded cells. The mass transfer coefficient, fractional mass left in the invaded cells, surface area and saturation were calculated and the results compiled. The relationship between the dimensioned and the non-dimensioned mass transfer coefficient is $\alpha^* = \frac{\alpha D}{L^2}$

2.3 RESULTS

This section presents the results obtained from 1050 simulation runs. The results show the influence of buoyancy forces and capillary heterogeneity on CO_2 leakage from a borehole after diffusion over a period of time. 105 simulation scenarios were created by varying the leak source size, correlation ratio, viscous, buoyancy and capillary forces. Each simulation scenario was repeated 10 times and averaged to obtain the final results. The emphasis is on the effective mass transfer coefficient, the fractional mass of CO_2 left in the invaded nodes, the relationship between the mass transfer coefficient, saturation and surface area of the CO_2. The summary of the values of the simulations are presented in tables and figures for clarity. The line source leakage and point source leakage show similar values.

Figure 2.3 shows the influence of varying the stratification styles on CO_2 diffusion history in the absence of buoyancy and viscous forces for the case of a line source leakage. Table 2.2 presents the summary values. Figures 2.4 and 2.5 show the plots for both line and point source leakages. The results are similar. For the unstructured media (vertical correlation length of 1 and a correlation ratio of 1), the fractional mass left is approximately 0.16. An increase in the vertical correlation length for the same correlation ratio of 1 show an increase in the fractional mass left to ~ 0.2 for the vertical correlation length of 10 and 50 at the end of the diffusion period in the domain because adjacent cells have similar spanning pressures and are filled up before reaching the percolation threshold. As the correlation ratio begins to increase for

all the vertical lengths considered (1, 10, 50), the fractional mass left in the domain begins to tend towards the same limiting value of ~0.04 for both line source and point source leakages.

In the plot of the mass transfer coefficient against the surface area, the data plots align in a linear fashion for all the vertical lengths and at all the correlation ratios considered. The correlation coefficient for the vertical correlation length of 1 is 0.9; for vertical correlation length of 10 is 0.996 and 1.00 for a vertical correlation length of 50 for both point and line source leak type. These values indicate that the mass transfer coefficient can be predicted from the surface area values with reasonable certainty.

The correlation coefficient of the mass transfer coefficient against saturation is shown in Table 2.3. The correlation coefficient for the vertical correlation length of 1 is 0.8044 which indicates a fairly strong relationship between the mass transfer coefficient and the saturation values. The correlation coefficient for the vertical correlation length of 1 is positive because, the unstructured medium has a significant influence on the other data sets. The large number of the mass transfer coefficient is as a result of the random nature in which the cells are invaded, so more CO_2 is able to get in before the percolation threshold is reached. As we begin to introduce some structure to it, the inverse relationship becomes more apparent. As the correlation ratio increases, the average saturation decreases because the adjacent cells are filled next to each other. The structured media shows a negative correlation coefficient which improves as the stratification increases.

The diffusion history of CO_2 in the presence of intermediate forces and no viscous force is shown in shown in Figure 2.6. The influence of varying the stratification styles on the fractional mass left in the invaded nodes in the presence of intermediate buoyancy (Bo = 0.1) and

no viscous forces for the case of a point leak source and line leak source is shown in Figure 2.8 and 2.9. Again, the point source and line source show similar results. For the unstructured media (i.e. a vertical correlation length of 1 and a correlation ratio of 1) the average fractional mass left in the domain is 0.02 which is an order of magnitude lower than when buoyancy forces were not present; as the CO_2 is being stretched vertically into narrow pores due to the buoyancy forces. For vertical correlation lengths of 10 and 50, though the buoyancy forces are still dominant, CO_2 fills adjacent blocks with similar spanning pressure which leads to an increase in the average fractional mass left in the domain as 0.04 and 0.06 respectively. As the correlation ratio increases from 1 to 10, there was an increase in the average fractional mass left for all the vertical correlation length considered for both point and line source leakages due to an increase in the vertical stacking in the presence of intermediate capillary heterogeneity effects. A further increase in the correlation ratio shows a decrease in the average fractional mass when the correlation ratio is 20 because at this point, capillary heterogeneity effects are much stronger than the buoyancy forces and the CO_2 is being stretched laterally into horizontal layers having similar spanning pressures. As the correlation ratio further increases, the average fractional mass left converged to about the same value of ~ .019 at a higher correlation. This result is true for both point and line source leakages. The summary values are presented in Table 2.4

For a correlation ratio of 1, it is observed that the mass transfer coefficient for a vertical correlation length of 1 (unstructured media) is ~ 180000. For a vertical correlation length of 10 and 50, the mass transfer coefficients are 80,000 and 60,000 respectively. Compared to Figures (2.4 and 2.5), buoyancy forces play a dominant role in the mass transfer coefficient as these figures are higher due to the increased surface area available for diffusion. As some structure is introduced, buoyancy forces play a less significant role; rather, the capillary heterogeneity seems

to be the dominant factor controlling the mass transfer coefficient. For a vertical correlation length of 1, there was a significant dip in the mass transfer coefficient and the slope remains gentle afterwards. For vertical correlation of 10 and 50, the mass transfer coefficient begins to tend to the same value of 100,000 which is also consistent with the figures plotted in the absence of buoyancy forces.

In the plot of mass transfer coefficient against the surface area in the presence of intermediate buoyancy forces (Bo = 0.1) and no viscous forces for both point and line source leakages; the results are similar. Again the data plots all align for all the vertical correlation lengths for both point and line source leakages and the correlation coefficients as shown in Table 2.5 show strong positive values. The mass transfer coefficient increases with the surface area as expected. The correlation coefficient when the vertical correlation length is 1 is 0.9727 and when the length is 10 is 0.987 and for 50 is 0.9269 for all the correlation ratios considered and for both source leakages.

Table 2.5 also shows the correlation coefficients of the mass transfer coefficient against saturation in the presence of intermediate buoyancy forces (Bo = 0.1) and no viscous forces for both line and point source leakages. When the vertical correlation length is 1, the correlation coefficient has a weak negative value and no apparent relationship exists among the data values. Indeed, the correlation coefficient is -0.4827 which confirms a weak dependence of either one on each other. However, as the vertical correlation length increases, an inverse relationship exists between the mass transfer coefficient and the saturation values for both source types. The correlation coefficient, when the vertical correlation length = 10 is -0.9724 and when the vertical correlation length is 50 is -0.9384.

The diffusion history of CO_2 in the presence of strong buoyancy forces (Bo =1) and no viscous forces on the fractional mass left in the domain is shown in Figure 2.9 and the summary results are presented in Tables 2.6. Figure 2.10 and 2.11 show the plots for both line and point source leakage respectively. Here again, the results are similar. For an unstructured media of vertical correlation length of 1, the average fractional mass left in the domain is 0.005 since the CO_2 was initially stretched into narrow vertical pores as a result of strong buoyancy forces resulting in lower saturation as it reaches the percolation threshold. The average fractional mass increases as the vertical correlation length increases to ~ 0.007 and ~ 0.008 for vertical correlation length of 10 and 50 respectively as a result of capillary heterogeneity effects forcing the CO_2 to invade blocks with similar spanning pressures laterally. As the correlation ratio increases to 10, there is an increase in the average fractional mass left for all the vertical correlation lengths. The rise was highest for vertical correlation of 10. It forms a small plateau when in the transition between 10 and 20 and then drops significantly; again due to stronger capillary heterogeneity effects. All three lengths tend towards a value of ~ 0.013 as the correlation ratio increases to 100. These results are true for both point and line source leakages.

The plot of mass transfer coefficient against the correlation ratio shows a similar result for both point and line leak source. For a correlation ratio of 1; when the vertical correlation ratio is 1, the mass transfer coefficient is ~280000. When the vertical correlation length is increased to 10, the mass transfer coefficient decreased to ~220000 and a further decrease to ~190000 when the vertical correlation coefficient is increased to 50. Compared to Bo = 0 and Bo = 0.1, the effect of buoyancy forces is strongly pronounced on the mass transfer coefficient. As the correlation ratio increases, there was an initial dip in the values of the mass transfer coefficient and then it steadily began to climb. Again, this is tightly interwoven with the available surface

area; since an initial increase in correlation ratio reduces the surface area available for diffusion as a result of competing buoyancy and capillary heterogeneity effects. However, at higher stratification, capillary heterogeneity effects dominate leading to an increased surface area which consequently increases the rate of mass transfer. For vertical correlation length of 1 and 10, the values at a correlation ratio of 50 and 100 are approximately the same. For vertical correlation of 50, it appears the stratification plays a marked increase in the value of the mass transfer coefficient when compared with the other vertical lengths.

Similarly when the mass transfer coefficient values are correlated with the surface area values as shown in Table 2.7, strong positive values were obtained. Indeed, the correlation coefficient when vertical correlation coefficient is 1 is 0.9868; when the vertical correlation lengths are 10 and 50; the correlation coefficients are 0.9991 and 0.9257 respectively for both point and line source leakage types. When mass transfer coefficient values are correlated against saturation, the vertical correlation length of 1 show a very weak relationship as the correlation coefficient is -0.5795 but shows a very strong relationship for increasing vertical correlation length.

For a vertical correlation length of 1, the presence of viscous forces introduces some nuances into the values obtained for the average fractional mass left at the end of the diffusion period as shown in Figure 2.12. The summary values are presented in Table 2.8. As seen in Figure 2.13, In the absence of buoyancy forces for the unstructured medium, the average fractional mass left is ~0.23 which is higher than when no viscous or buoyancy force was present because the viscous forces lead to pooling of CO_2 around the source which decreases CO_2 surface area and increases the saturation value. In the presence of intermediate buoyancy forces, the average fractional mass left peaked at a correlation ratio of 10 due to increase in vertical

stacking and not too competitive capillary effects but then dropped slightly at 20 as the capillary effects become more dominant and then even more as the correlation ratios increase to 50 and 100. When buoyancy forces were present, the values were approximately the same when the medium was unstructured

When Bo = 1 and the correlation ratio is 1, the mass transfer coefficient is ~250,000 which is similar to the value obtained when no viscous force was present for the same strength of Bond number. For increasing values of correlation ratios the trend appears to be the same but decreased significantly at a high correlation ratio due to stronger capillary effects. Similarly, when Bo = 0.1 there appears to be no difference in the mass transfer coefficient values when compared with the case when viscous forces were not considered. However, for the case where B = 0, the mass transfer coefficient is ~ 150,000. There appears to be a slight decrease in the mass transfer coefficient when compared with the case of no viscous forces. As the correlation ratio begins to increase however, the mass transfer coefficient begins to hover about the same value of ~ 80,000.

Generally, in the presence of increased buoyancy forces, the surface area increases due to the vertical fingering thereby increasing the mass transfer coefficient. Table 2.9 shows the correlation coefficients for the increasing Bond numbers. For all the Bond numbers considered, the correlation coefficients between the average mass transfer coefficient and the surface area are strong positive values. Likewise for the saturation, the correlation coefficient in the absence of Buoyancy forces is a strong positive value. When Bo = 0.1, there exists a weak negative correlation coefficient and the value further improves as the Bond number increases.

2.4 SUMMARY AND DISCUSSION

We examined the effective mass transfer coefficient of a CO_2 plume in shallow aquifer resulting from a well bore leak, subject to capillary, viscous and buoyancy forces by using an MIP approach to simulate the invasion of CO_2 into a medium initially saturated with water. Following invasion, the diffusion of gas into and through the aqueous phase was simulated using a block-centered finite difference model. 105 different simulation scenarios were created and the capillary heterogeneity, buoyancy and viscous forces were systematically varied to mimic the range of soil systems found in nature.

Results show that an increase in saturation does not result in an increase in mass transfer coefficient rather, the surface area, which in turn is controlled by the interplay of capillary heterogeneity effects and buoyancy forces, control the average mass transfer coefficient and the fractional mass left. We further correlated the mass transfer coefficient with the average surface area and saturation and we found that a very strong positive correlation coefficient exists between the surface area of the CO_2 and mass transfer coefficient and a weak negative correlation coefficient exists between the average mass transfer coefficient and saturation exists, which improves with increasing stratification and increasing buoyancy forces.

Table 2.1: Simulation variables and values for Modified Invasion Percolation

Viscous Scaling Number (VSN)	0, 250
Leak Source Sizes	1, 102
Vertical Correlation Lengths	1, 10, 50
Correlation Ratios	1, 10, 20, 50, 100
Bond Number	0, 0.1, 1

VL = 1, CR = 1

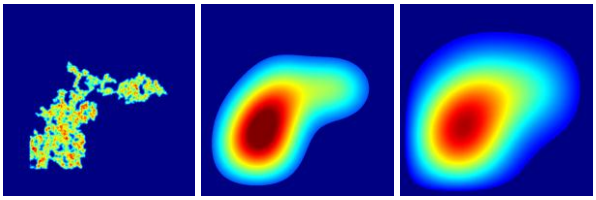

VL = 1, CR = 10

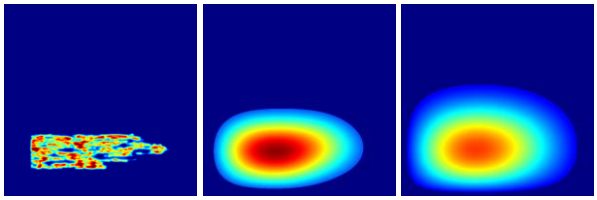

VL = 1, CR =20

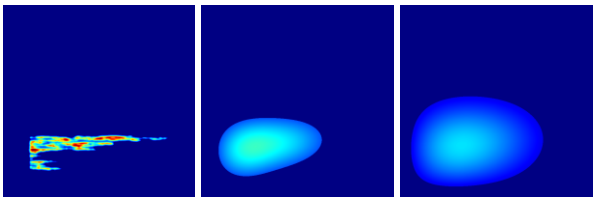

VL = 1, CR = 50

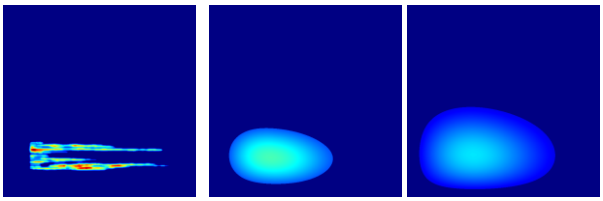

VL = 1, CR = 100

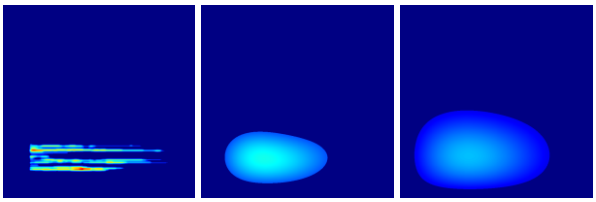

VL = 10, CR = 1

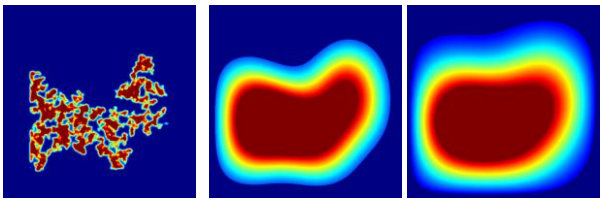

VL = 10, CR = 10

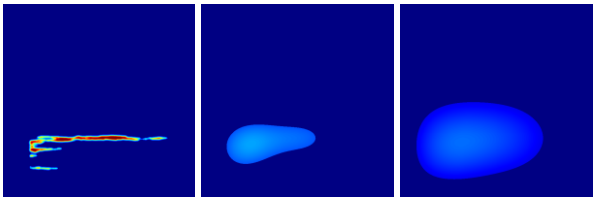

VL = 10, CR = 20

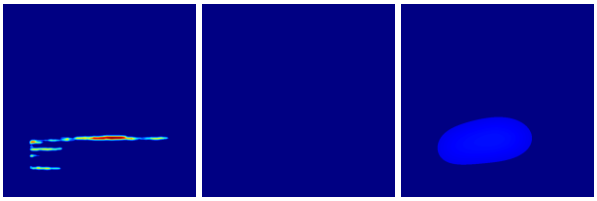

VL = 10, CR = 50

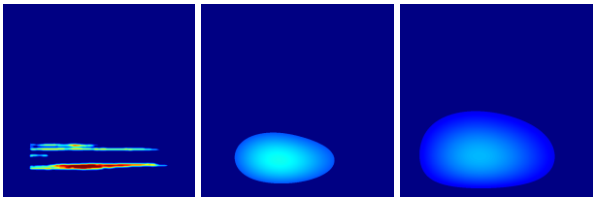

VL = 10, CR = 100

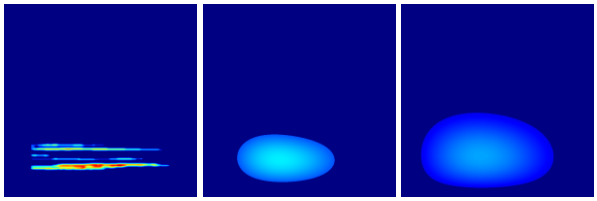

VL = 50, CR = 1

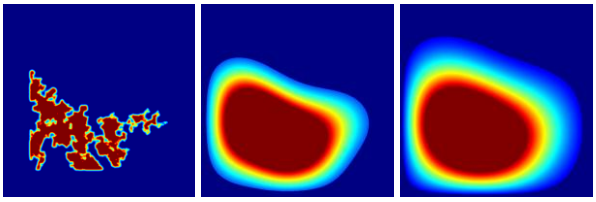

VL = 50, CR = 10

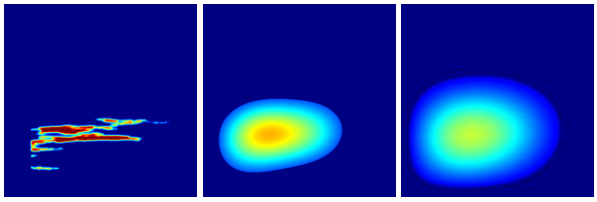

VL = 50, CR = 20

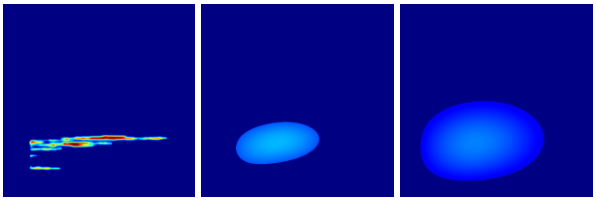

VL = 50, CR = 50

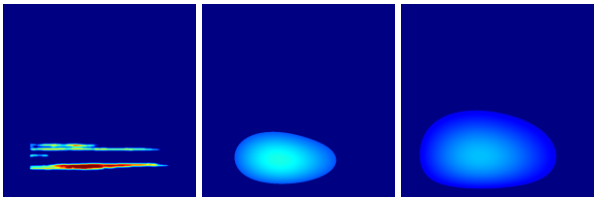

VL = 50, CR = 100

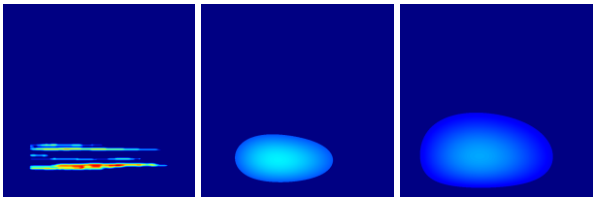

VL – Vertical Correlation Length**; CR –** Correlation Ratio

COLORBAR

INITIAL DIFFUSION:

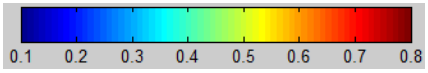

INTERMEDIATE DIFFUSION:

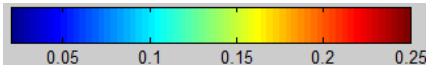

FINAL DIFFUSION:

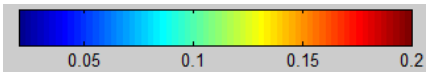

Figure 2.3: CO_2 diffusion history at the initial, intermediate and final time step when Bo = 0

VCL – Vertical Correlation Length; CR – Correlation Ratio

Table 2.2: Data values of the average fractional mass, average mass transfer coefficient, average surface area, average saturation for a line source leakage with Bo = 0 and VSN = 0

CR	Average Fractional Mass			Average Mass Transfer Coefficient			Average Surface Area			Average Saturation		
	VL 1	VL 10	VL 50	VL 1	VL 10	VL 50	VL 1	VL 10	VL 50	VL 1	VL10	VL 50
1	0.156	0.224	0.256	156100	48320	23426	0.974	0.333	0.173	0.140	0.208	0.218
10	0.076	0.108	0.122	96345	41150	32867	0.668	0.308	0.246	0.048	0.068	0.076
20	0.065	0.069	0.074	97113	46118	43218	0.671	0.360	0.332	0.040	0.042	0.045
50	0.045	0.048	0.049	107311	70502	68888	0.796	0.536	0.521	0.027	0.029	0.030
100	0.032	0.034	0.034	121170	97339	96382	0.934	0.744	0.738	0.020	0.021	0.021

CR – Correlation Ratio

Table 2.3: Data values of the correlation coefficient between the average mass transfer coefficient vs the average surface area and saturation for a line source leakage with Bo = 0 and VSN = 0

Correlation Coefficient	VL 1	VL 10	VL 50
Average Mass Transfer Coefficient vs Average Surface Area	0.8997	0.9962	0.9999
Average Mass Transfer Coefficient vs Average Saturation	0.8044	-0.4818	-0.7328

a)

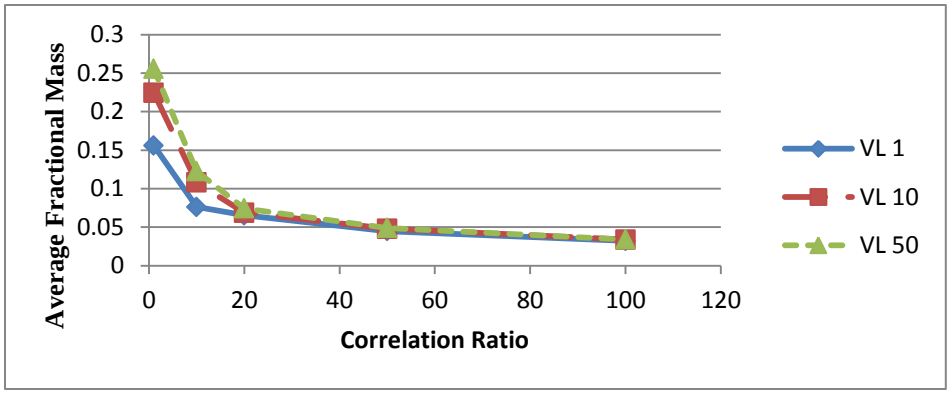

b)

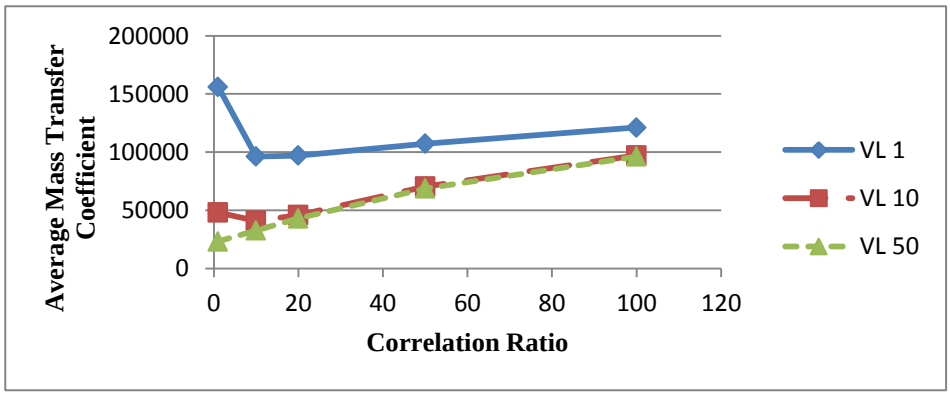

c)

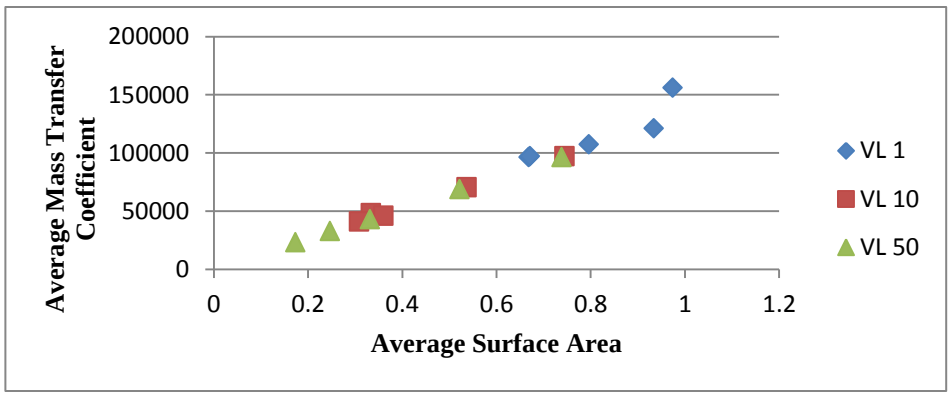

Figure 2.4: Line source leakage plots for vertical correlation length of 1,10 and 50 with Bo =0 and VSN = 0
(a) average fractional mass vs correlation ratio (b) average mass transfer coefficient vs correlation ratio (c) average mass transfer coefficient against average surface area

a}

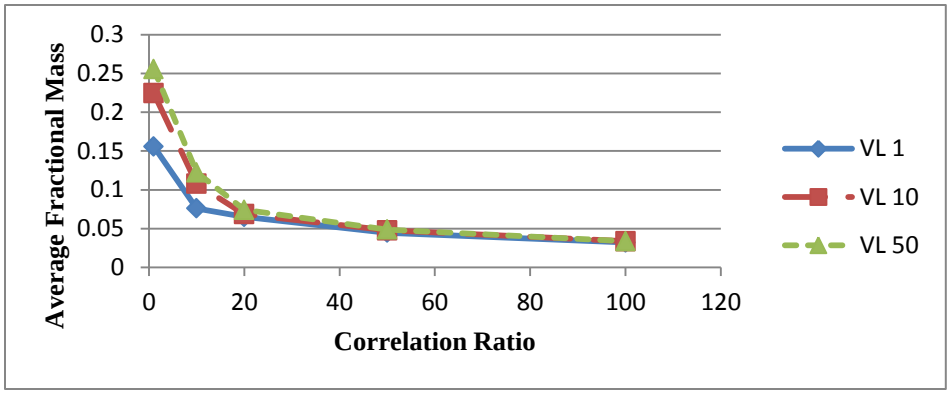

b)

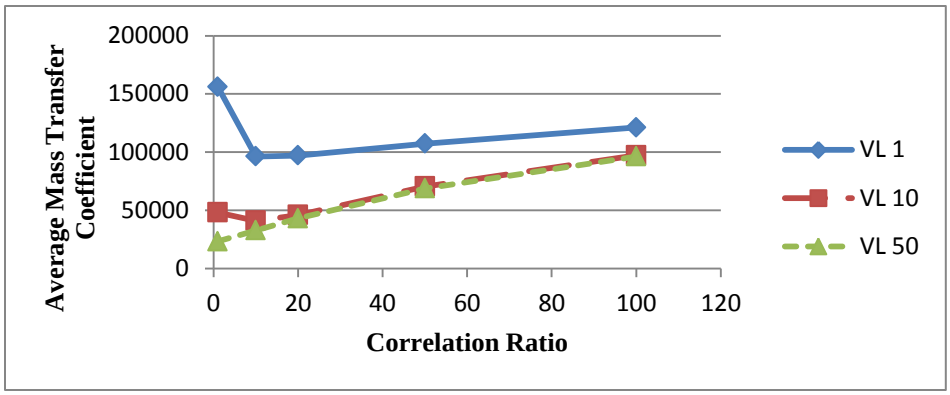

c)

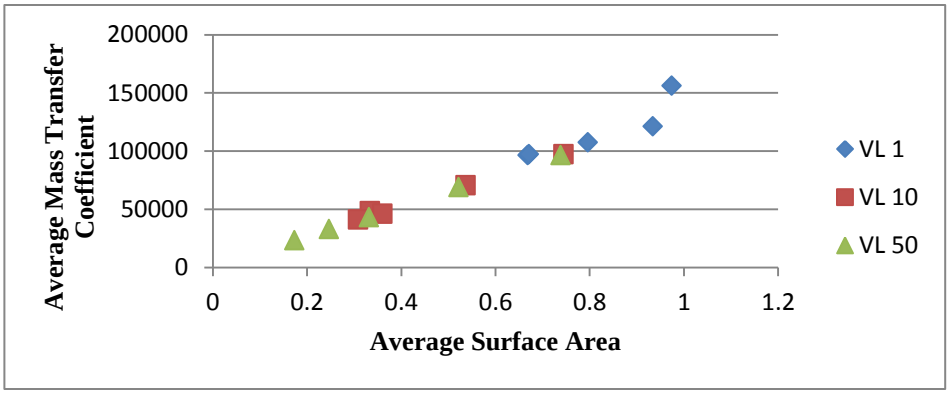

Figure 2.5: Point source leakage plots for vertical correlation length of 1,10 and 50 with Bo =0 and VSN = 0
(a) average fractional mass vs correlation ratio (b) average mass transfer coefficient vs correlation ratio (c) average mass transfer coefficient against average surface area
VL – Vertical Correlation Length

VL = 1, CR = 1

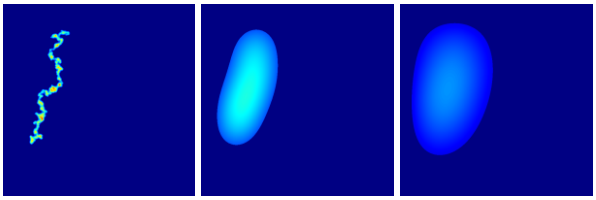

VL = 1, CR = 10

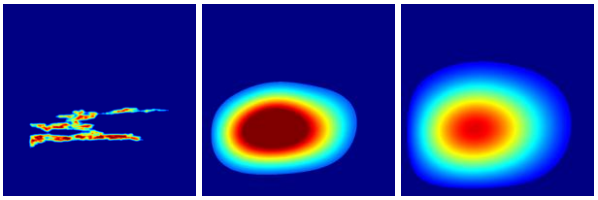

VL = 1, CR = 20

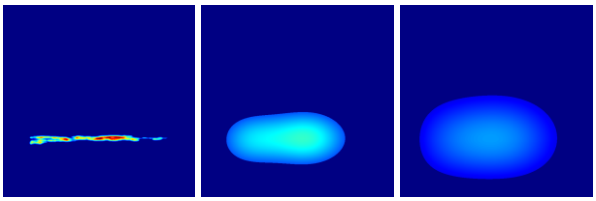

VL = 1, CR = 50

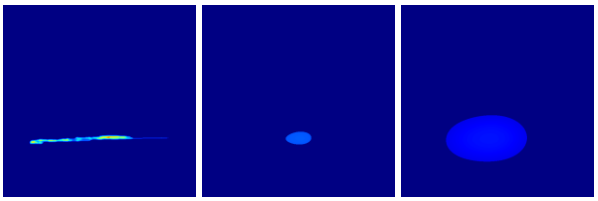

VL = 1, CR = 100

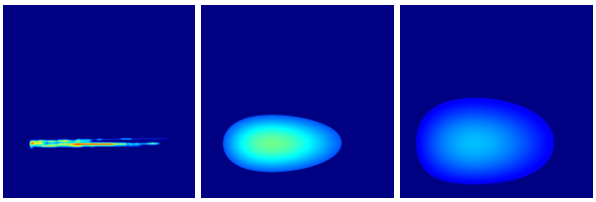

VL = 10, CR = 1

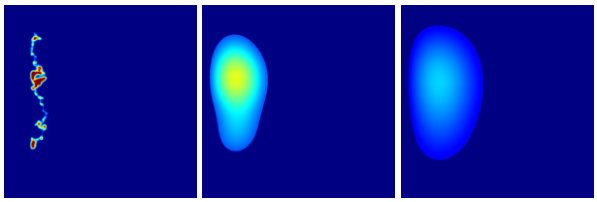

VL = 10, CR = 10

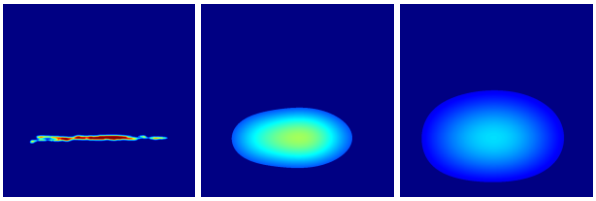

VL = 10, CR = 20

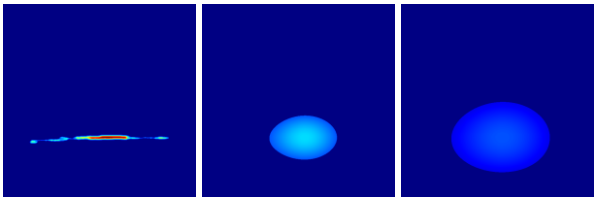

VL = 10, CR = 50

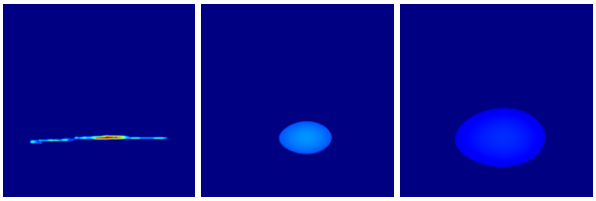

VL = 10, CR = 100

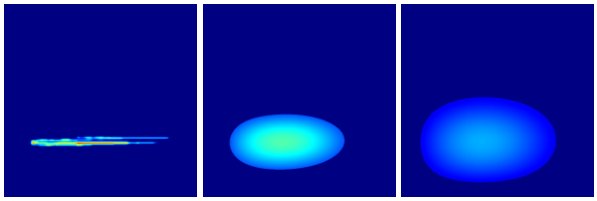

VL = 50, CR = 1

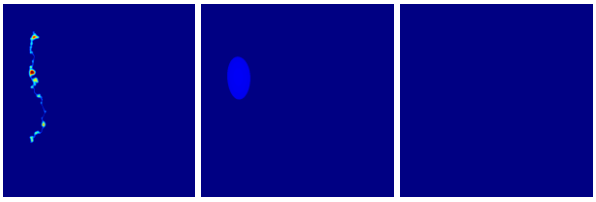

VL = 50, CR = 10

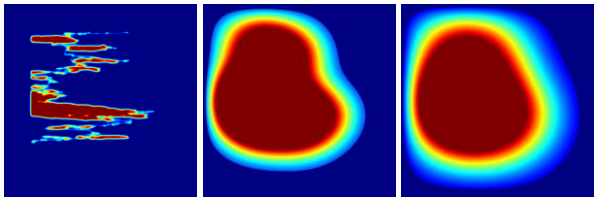

VL = 50, CR = 20

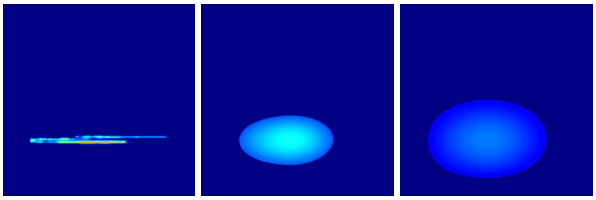

VL = 50, CR = 50

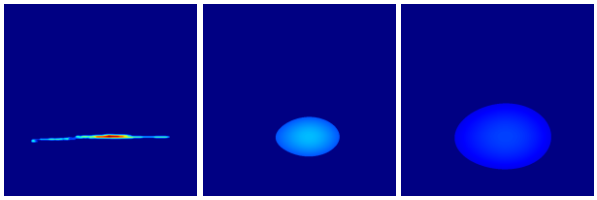

VL = 50, CR = 100

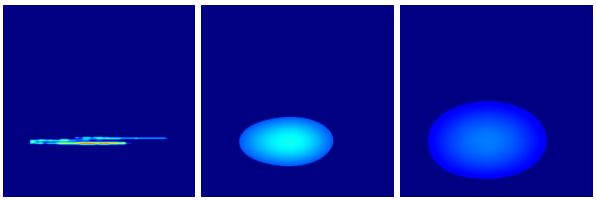

COLOR BAR

INITIAL DIFFUSION:

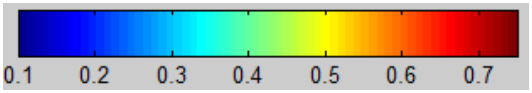

INTERMEDIATE DIFFUSION:

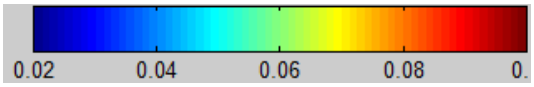

FINAL DIFFUSION:

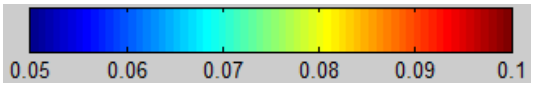

Figure 2.6: CO_2 diffusion history at the initial, intermediate and final time step when Bo = 0.1

VL – Vertical Correlation Length; CR – Correlation Ratio

Table 2.4: Data values of the average fractional mass, average mass transfer coefficient, average surface area, average saturation for a line source leakage with Bo = 0.1 and VSN = 0

CR	Average Fractional Mass			Average Mass Transfer Coefficient			Average Surface Area			Average Saturation		
	VL 1	VL 10	VL 50	VL 1	VL 10	VL 50	VL 1	VL 10	VL 50	VL 1	VL10	VL 50
1	0.021	0.037	0.059	181760	77834	65860	1.265	0.681	0.671	0.013	0.022	0.031
10	0.071	0.067	0.075	105882	56849	55258	0.719	0.444	0.477	0.052	0.041	0.047
20	0.052	0.054	0.049	100592	59020	65927	0.716	0.484	0.535	0.031	0.032	0.028
50	0.020	0.028	0.033	108930	90054	92077	0.833	0.721	0.730	0.012	0.016	0.018
100	0.016	0.019	0.019	126190	98264	102572	0.989	0.808	0.842	0.010	0.011	0.011

CR – Correlation Ratio

Table 2.5: Data values of the correlation coefficient between the average mass transfer coefficient vs the average surface area and saturation for a line source leakage with Bo = 0.1 and VSN = 0

Correlation Coefficient	VL 1	VL 10	VL 50
Average Mass Transfer Coefficient vs Average Surface Area	0.9727	0.9870	0.9269
Average Mass Transfer Coefficient vs Average Saturation	-0.4827	-0.9724	-0.9384

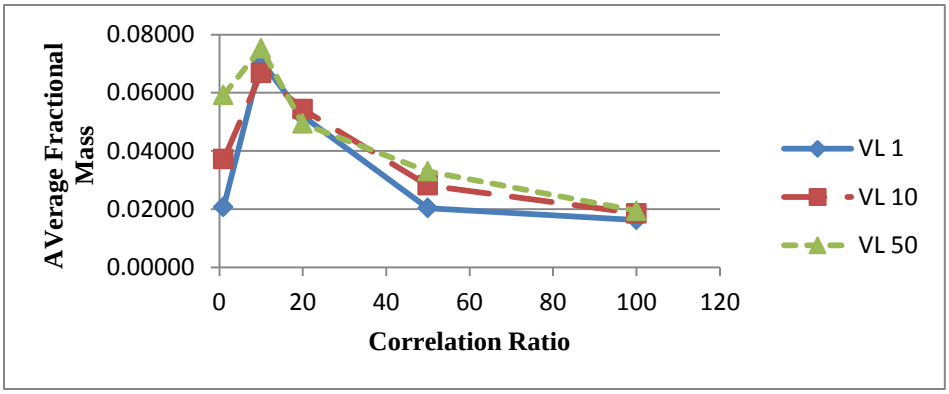

b)

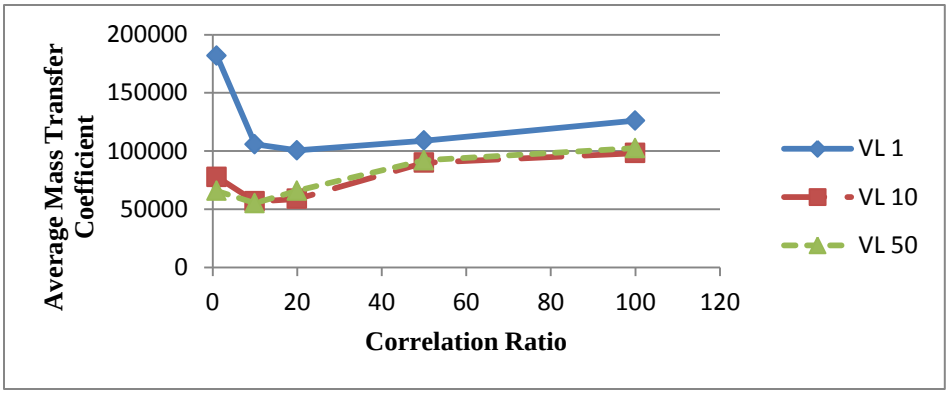

c)

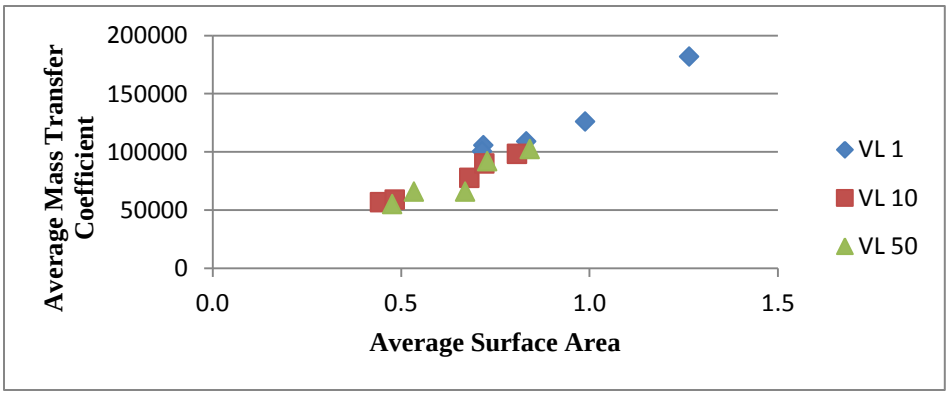

Figure 2.7: Line source leakage plots for vertical correlation length of 1,10 and 50 with Bo = 0.1 and VSN = 0
(a) average fractional mass vs correlation ratio (b) average mass transfer coefficient vs correlation ratio (c) average mass transfer coefficient against average surface area

a)

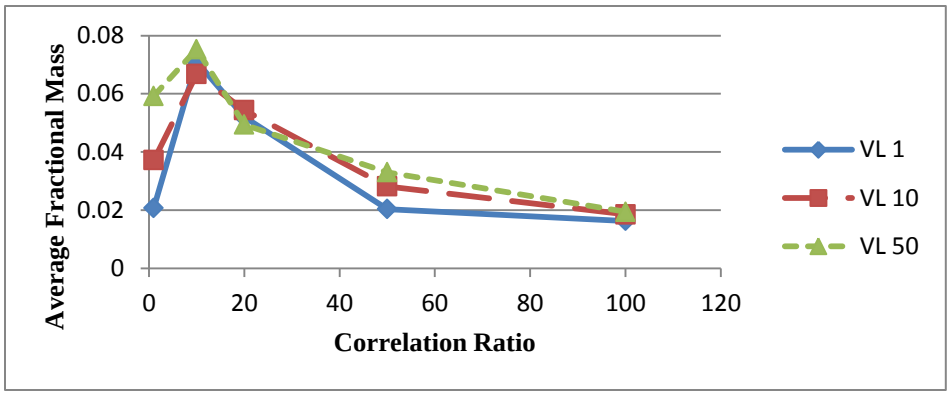

b)

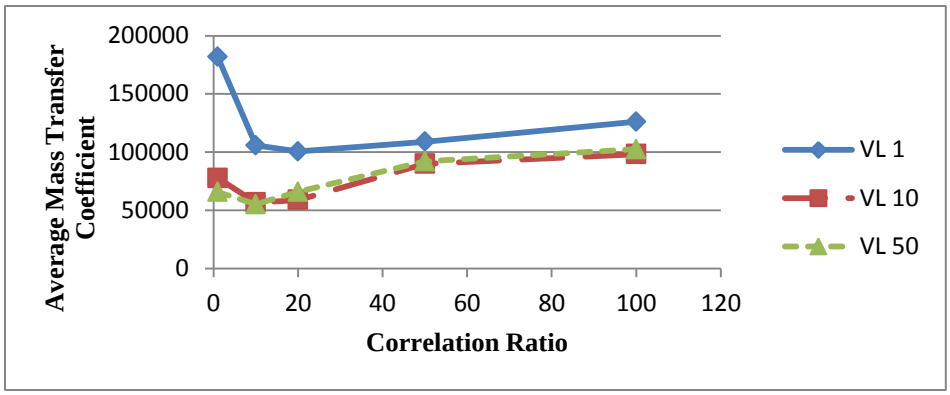

c)

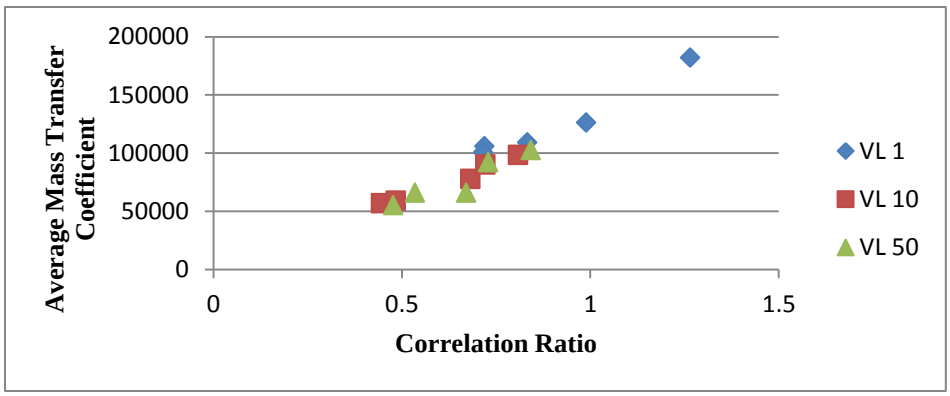

Figure 2.8: Point source leakage plots for vertical correlation length of 1,10 and 50 with Bo = 0.1 and VSN = 0
(a) average fractional mass vs correlation ratio (b) average mass transfer coefficient vs correlation ratio (c) average mass transfer coefficient against average surface area
VL – Vertical Correlation Length

VL = 1, CR = 1

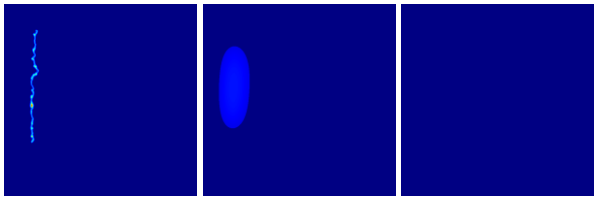

VL = 1, CR = 10

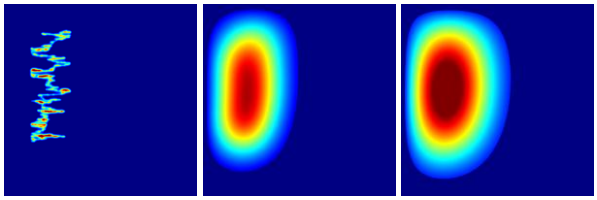

VL = 1, CR = 20

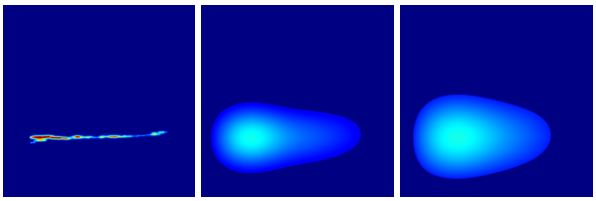

VL = 1, CR = 50

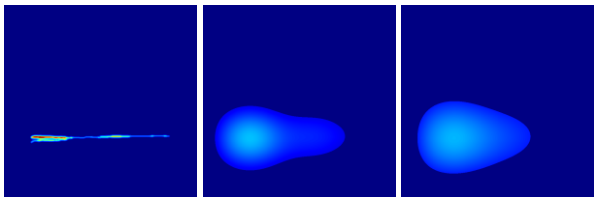

VL = 1, CR = 100

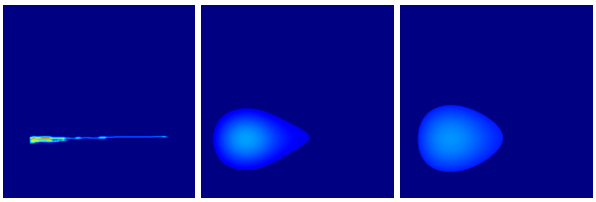

VL = 10, CR = 1

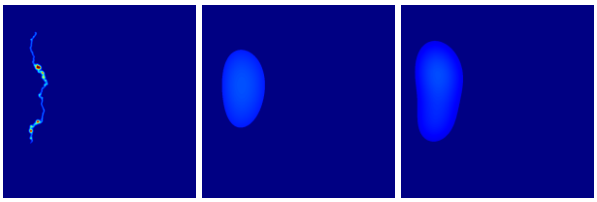

VL = 10, CR = 10

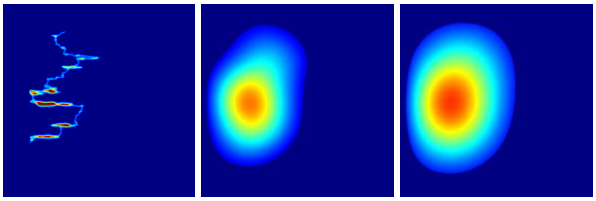

VL = 10, CR = 20

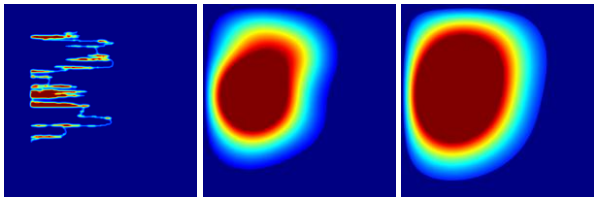

VL = 10, CR = 50

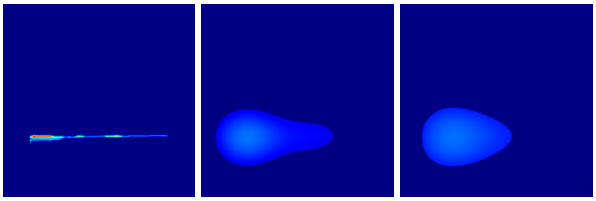

VL = 10, CR = 100

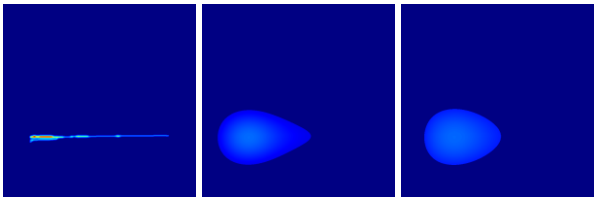

VL = 50, CR = 1

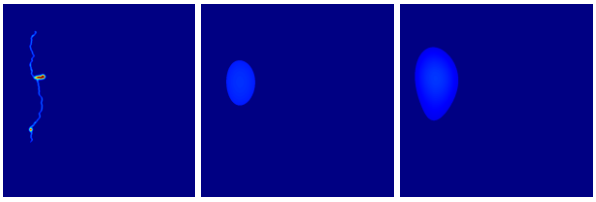

VL = 50, CR = 10

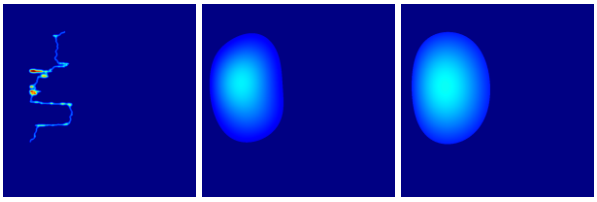

VL = 50, CR = 20

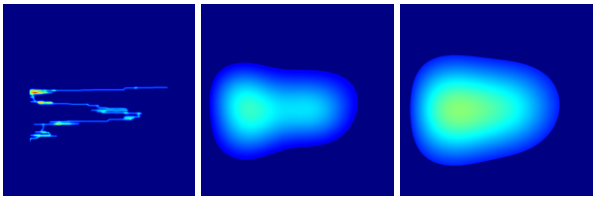

VL = 50, CR = 50

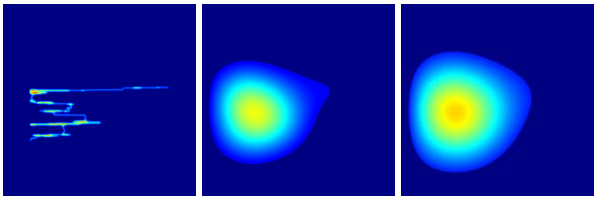

VL = 50, CR = 100

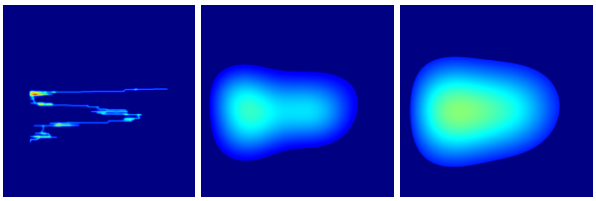

COLORBAR

INITIAL DIFFUSION:

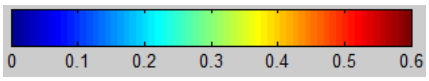

INTERMEDIATE DIFFUSION:

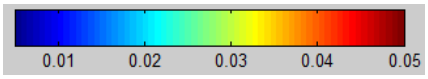

FINAL DIFFUSION:

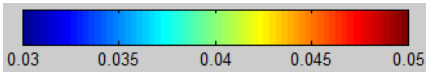

Figure 2.9: CO_2 diffusion history at the initial, intermediate and final time step when Bo= 1

VL – Vertical Correlation Length; CR – Correlation Ratio

Table 2.6: Data values of the average fractional mass, average mass transfer coefficient, average surface area, average saturation for a line source leakage with Bo =1 and VSN = 0

CR	Average Fractional Mass			Average Mass Transfer Coefficient			Average Surface Area			Average Saturation		
	VL 1	VL 10	VL 50	VL 1	VL 10	VL 50	VL 1	VL 10	VL 50	VL 1	VL10	VL 50
1	0.005	0.007	0.009	267260	213003	187388	2.309	1.898	1.944	0.003	0.004	0.005
10	0.026	0.030	0.021	179980	101600	117128	1.322	0.903	1.167	0.019	0.020	0.013
20	0.024	0.029	0.016	150670	108245	130186	1.192	0.938	1.249	0.017	0.021	0.012
50	0.019	0.015	0.015	137190	141712	182030	1.115	1.225	1.631	0.011	0.009	0.011
100	0.012	0.011	0.013	161690	170600	231160	1.331	1.485	1.905	0.007	0.007	0.010

CR – Correlation Ratio

Table 2.7: Data values of the correlation coefficient between the average mass transfer coefficient vs the average surface area and saturation for a line source leakage with Bo = 1 and VSN = 0

Correlation Coefficient	VL 1	VL 10	VL 50
Average Mass Transfer Coefficient vs Average Surface Area	0.9868	0.9991	0.9257
Average Mass Transfer Coefficient vs Average Saturation	-0.57948	-0.9378	-0.5090

a)

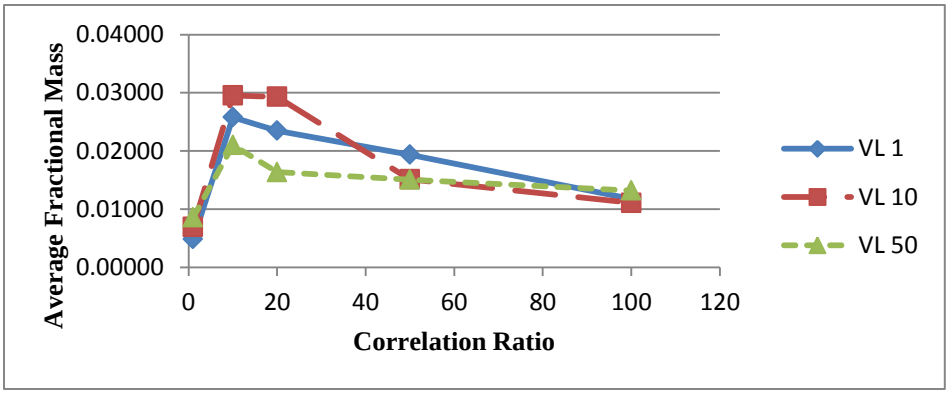

b)

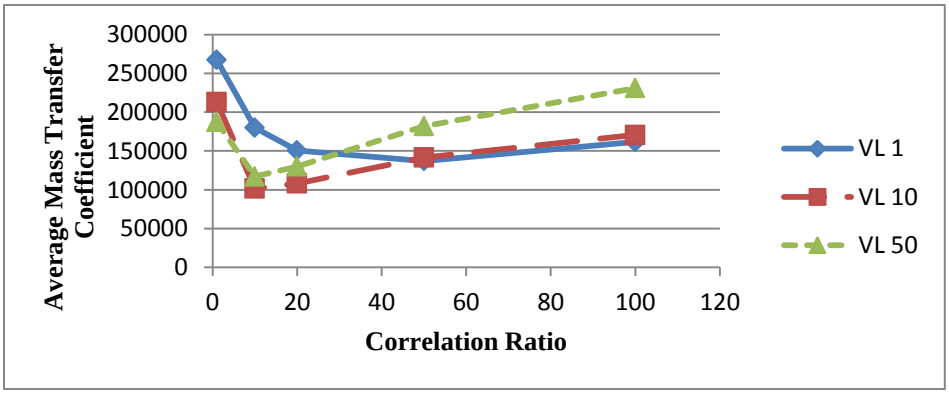

c)

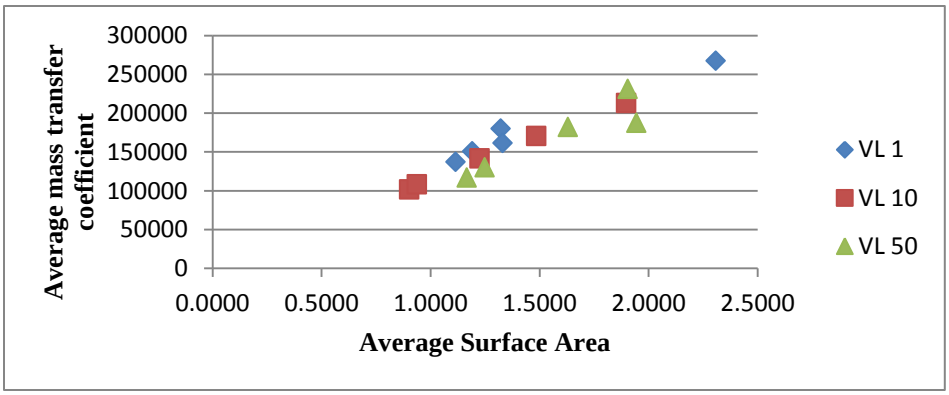

Figure 2.10: Line source leakage plots for vertical correlation length of 1,10 and 50 with Bo = 1 and VSN = 0
(a) average fractional mass vs correlation ratio (b) average mass transfer coefficient vs correlation ratio (c) average mass transfer coefficient against average surface area
VL – Vertical Correlation Length

a)

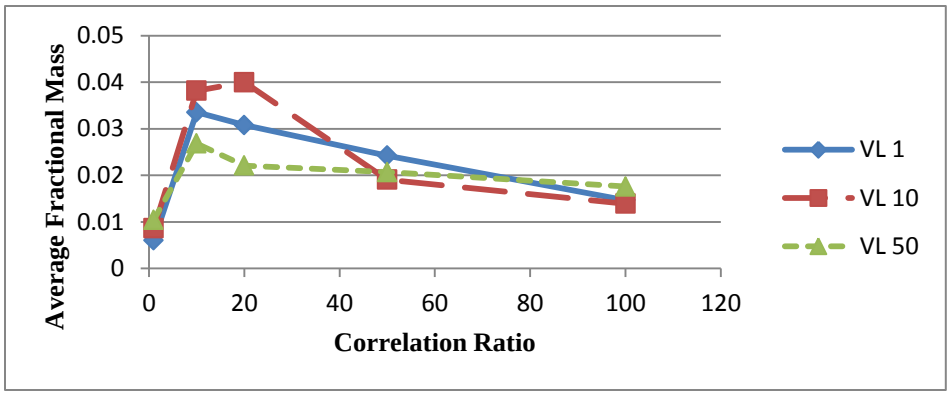

b)

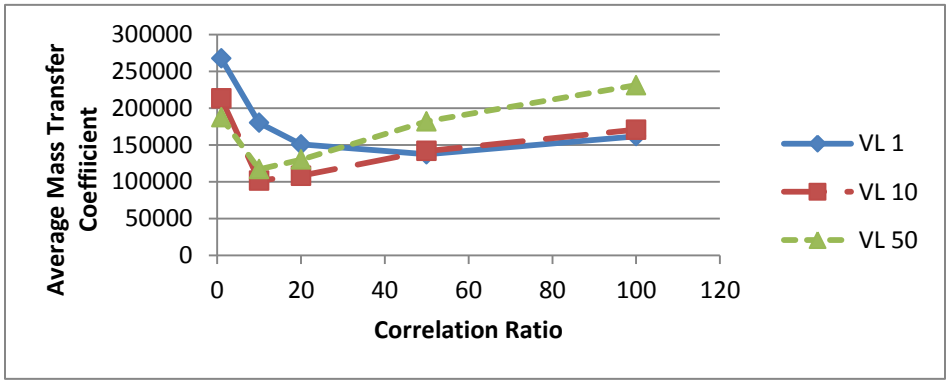

c)

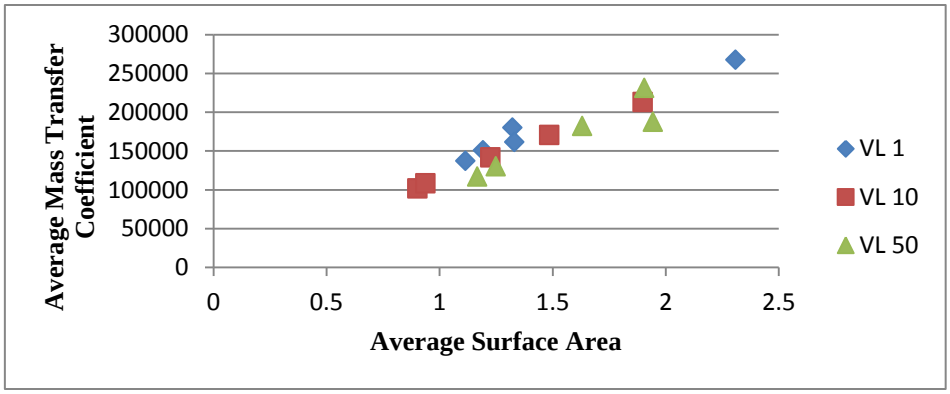

Figure 2.11: Point source leakage plots for vertical correlation length of 1,10 and 50 with Bo = 1 and VSN = 0
(a) average fractional mass vs correlation ratio (b) average mass transfer coefficient vs correlation ratio (c) average mass transfer coefficient against average surface area
VL – Vertical Correlation Length

VL = 1, CR = 1, Bo = 0

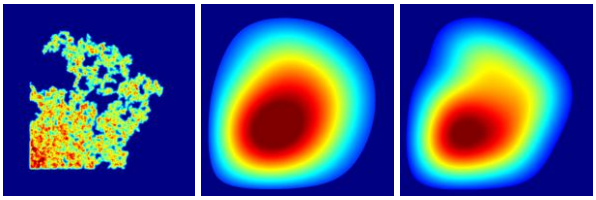

VL = 1, CR = 10, Bo = 0

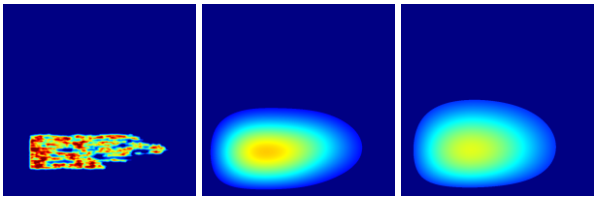

VL = 1, CR = 20, Bo = 0

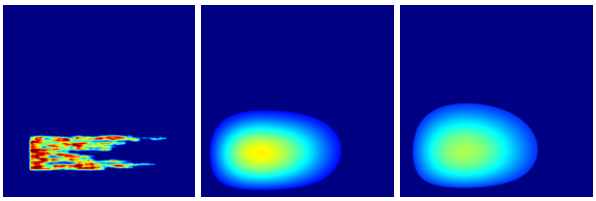

VL = 1, CR = 50, Bo = 0

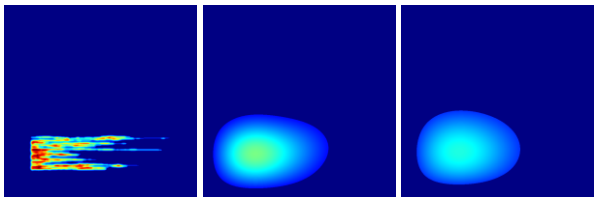

VL = 1, CR = 100, Bo = 0

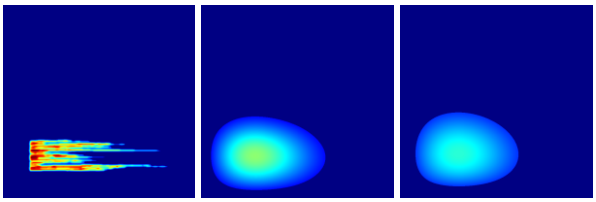

VL = 1, CR = 1, Bo = 0.1

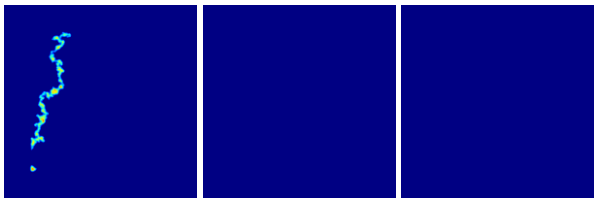

VL = 1, CR = 10, Bo = 0.1

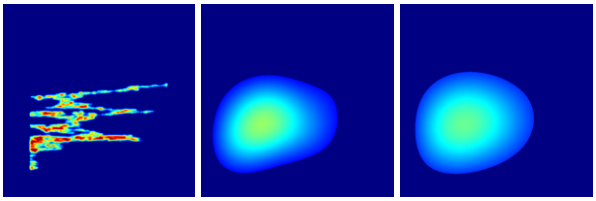

VL = 1, CR = 20, Bo = 0.1

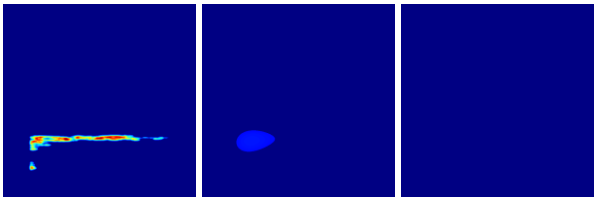

VL = 1, CR = 50, Bo = 0.1

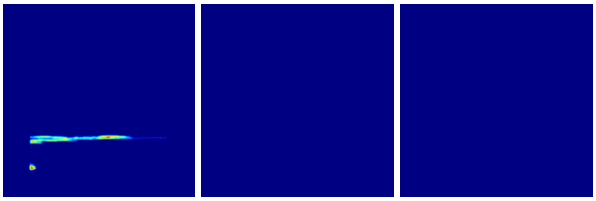

VL = 1, CR = 100, Bo = 0.1

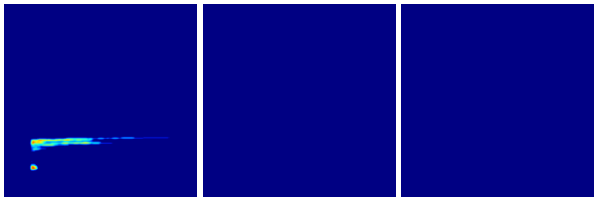

VL = 1, CR = 1, Bo = 1

VL = 1, CR = 10, Bo = 1

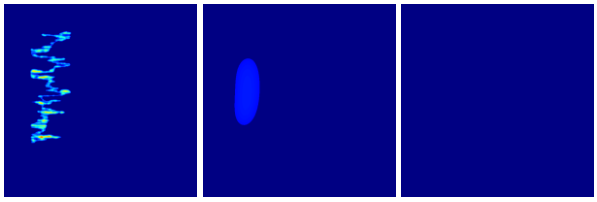

VCL = 1, CR = 20, Bo = 1

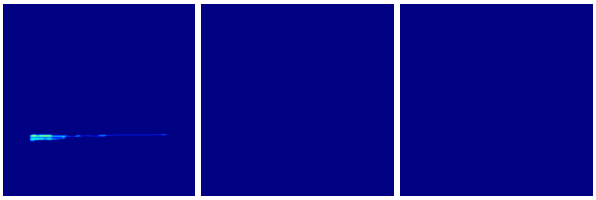

VCL = 1, CR = 50, Bo = 1

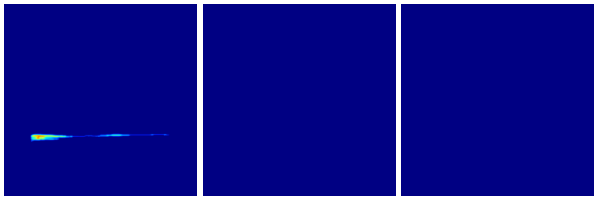

VCL = 1, CR = 100, Bo = 1

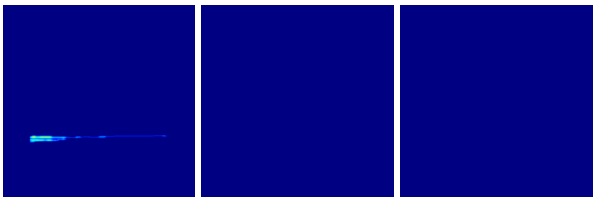

INITIAL DIFFUSION:

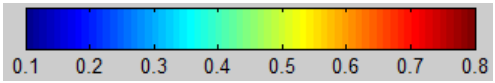

INTERMEDIATE DIFFUSION:

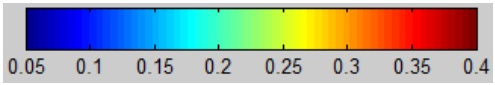

FINAL DIFFUSION:

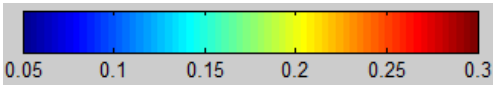

Figure 2.12: CO_2 diffusion history at the initial, intermediate and final time step when VSN = 250;
VL – Vertical Correlation Length; CR – Correlation Ratio

Table 2.8: Data values of the average fractional mass, average mass transfer coefficient, average surface area, average saturation for a line source leakage with Bo = 0, 0.1 and 1 and VSN = 250

CR	Average Fractional Mass			Average Mass Transfer Coefficient			Average Surface Area			Average Saturation		
	0	**0.1**	**1**	**0**	**0.1**	**1**	**0**	**0.1**	**1**	**0**	**0.1**	**1**
1	0.226	0.022	0.027	142320	167650	258930	0.887	1.199	2.160	0.228	0.015	0.028
10	0.120	0.099	0.026	85385	108143	179980	0.582	0.721	1.319	0.075	0.079	0.019
20	0.106	0.070	0.026	82548	94247	158990	0.572	0.668	1.204	0.065	0.044	0.018
50	0.085	0.033	0.026	85102	94809	130190	0.610	0.720	1.059	0.050	0.021	0.017
100	0.077	0.024	0.015	88653	104897	141460	0.655	0.821	1.177	0.045	0.014	0.008

Table 2.9: Data values of the correlation coefficient between the average mass transfer coefficients vs the average surface area and saturation for a line source leakage for various Bond numbers

Correlation Coefficient	Bo = 0	Bo = 0.1	Bo = 1.0
Average Mass Transfer Coefficient vs Average Surface Area	0.9847	0.9765	0.9832
Average Mass Transfer Coefficient vs Average Saturation	0.9770	-0.3097	0.8584

a)

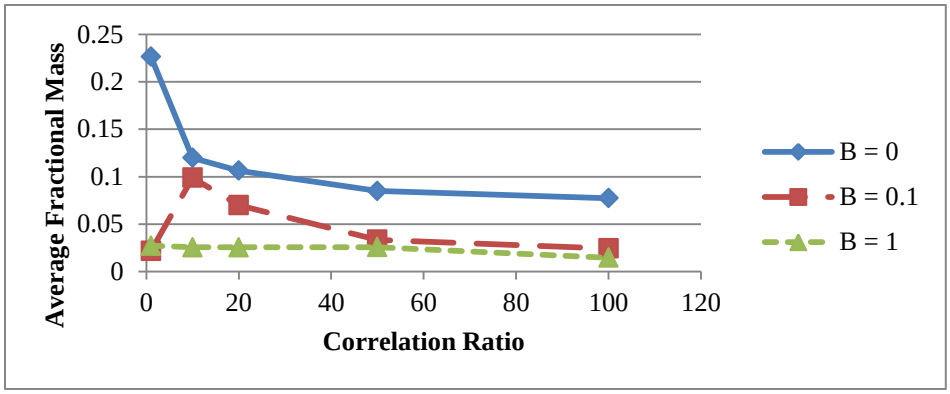

b)

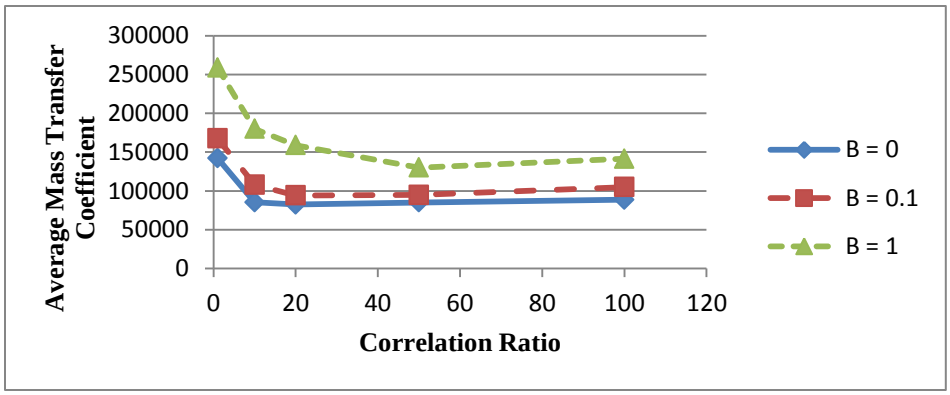

c)

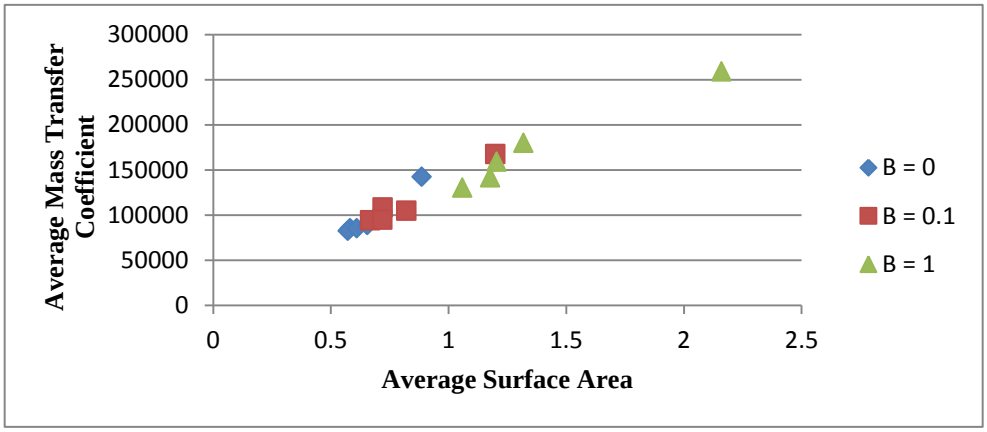

Figure 2.13: Line source leakage plots for Bo =0, 0.1, 1 with Bo = 1 and VSN = 250 (a) average fractional mass vs correlation ratio (b) average mass transfer coefficient vs correlation ratio (c) average mass transfer coefficient against average surface area

LIST OF REFERENCES

2.4 REFERENCES

Brook, G. A., Folkoff, M. E., & Box, E. O. (1983). A world model of soil carbon dioxide. *Earth Surface Processes and Landforms*, *8*(1), 79–88. doi:10.1002/esp.3290080108

Burnside, N. M., Shipton, Z. K., Dockrill, B., & Ellam, R. M. (2013). Man-made versus natural CO2 leakage: A 400 k.y. history of an analogue for engineered geological storage of CO2. *Geology*, *41*(4), 471–474. doi:10.1130/G33738.1

Buyanovsky, G. A., & Wagner, G. H. (1983). Annual Cycles of Carbon Dioxide Level in Soil Air1. *Soil Science Society of America Journal*, *47*(6), 1139. doi:10.2136/sssaj1983.03615995004700060016x

Carslaw, H. S., & Jaeger, J. J. C. (1986). *Conduction of Heat in Solids* (p. 510). Clarendo Press. Retrieved from http://books.google.com/books/about/Conduction_of_Heat_in_Solids.html?id=y20sAAAAYAAJ&pgis=1

Dobossy, M. E., Celia, M. a., & Nordbotten, J. M. (2011). An efficient software framework for performing industrial risk assessment of leakage for geological storage of CO2. *Energy Procedia*, *4*, 4207–4214. doi:10.1016/j.egypro.2011.02.368

Edlmann, K., Haszeldine, S., & McDermott, C. I. (2013). Experimental investigation into the sealing capability of naturally fractured shale caprocks to supercritical carbon dioxide flow. *Environmental Earth Sciences*, *70*(7), 3393–3409. doi:10.1007/s12665-013-2407-y

Elena, R. O. (2011). SITE SELECTION AND CHARACTERIZATION FOR CO 2 STORAGE CAPACITY ESTIMATION, *12*, 263–272.

Holloway, S. (2007). Carbon dioxide capture and geological storage. *Philosophical Transactions. Series A, Mathematical, Physical, and Engineering Sciences*, *365*(1853), 1095–107. doi:10.1098/rsta.2006.1953

Holt, R. M. (2003). Influence of centrifugal forces on phase structure in partially saturated media. *Geophysical Research Letters*, *30*(13), 1692. doi:10.1029/2003GL017340

Kiefer, R. (1990). SOIL CARBON DIOXIDE CONCENTRATIONS AND CLIMATE IN A HUMID SUBTROPICAL ENVIRONMENT. *The Professional Geographer*, *42*(2), 182–194. doi:10.1111/j.0033-0124.1990.00182.x

Konikow, L., & Bredehoeft, J. (1978). *Computer model of two-dimensional solute transport and dispersion in ground water*. Retrieved from http://pubs.usgs.gov/twri/twri7c2/

Lewicki, J. L., Birkholzer, J., & Tsang, C.-F. (2006). Natural and industrial analogues for leakage of CO2 from storage reservoirs: identification of features, events, and processes and lessons learned. *Environmental Geology*, *52*(3), 457–467. doi:10.1007/s00254-006-0479-7

Roecker, F. (2012). INFLUENCE OF CAPILLARY HETEROGENEITY ON LEAKAGE OF CO2 FROM A BOREHOLE A Thesis presented in partial fulfillment of requirements for the degree of Masters of Engineering Science in the Department of Geology and Geological Engineering The University of Mis, (May).

Šimůnek, J., & Suarez, D. L. (1993). Modeling of carbon dioxide transport and production in soil: 1. Model development. *Water Resources Research*, *29*(2), 487–497. doi:10.1029/92WR02225

Song, J., & Zhang, D. (2013). Comprehensive review of caprock-sealing mechanisms for geologic carbon sequestration. *Environmental Science & Technology*, *47*(1), 9–22. doi:10.1021/es301610p

Wilkinson, D., & Willemsen, J. F. (1983). Invasion percolation : a new form of percolation theory, *16*(May), 3365–3376.

CHAPTER 3

EFFECTIVE DIFFUSION TORTUOSITY IN ASYMMETRIC POROUS MEMBRANES

3.1 INTRODUCTION

The description of flow through porous media has been an active area of research across many disciplines due to its broad range of applications. There are a wide variety of materials, both natural and artificial that can be readily described as porous. Examples include rubber, ceramics, lungs, kidneys, fissured rock, soils, filters and membranes(Bear & Bachmat, 1990). As diverse as these examples are, so are their uses and applications.

Several flow problems; such as flows in chemical reactors, oil and gas production in petroleum reservoirs and separation processes using membranes; can be described and analyzed as porous media. Loosely, all materials can be considered porous(Coutelieris & Delgado, 2012; Darby, 2001) i.e. the solid materials contain significant open spaces around them such as to allow fluid pass through and around them. In many engineering applications and analyses, however, require more specific and restrictive definitions. These restrictions require that the smallest dimension of the non-solid space be large enough to contain fluid particles, the non-solid space within the matrix be interconnected and that the dimensions of these non-solid spaces be so small that, the orientation of interfaces between two fluids, is largely dominated by interfacial forces.(Corey, 1994)

Among the several applications of porous media, the research into separation processes involving membranes has continued to increase over the years. This is because membrane technology is relatively new, cheap and makes use of efficient technology. Membranes control the flow of various chemicals in a selective manner by acting as a barrier between two phases. They typically have lateral dimensions greater than thickness through which mass transfer may occur under a wide variety of driving forces. The driving forces causing the flow are sometimes used in the classification of membranes. These driving forces include pressure difference as in ultrafiltration, microfiltration; temperature difference as in membrane distillation; concentration difference as in dialysis and membrane extraction; electric potential difference as in electro-dialysis. Another classification is based on the structure of the membranes – homogeneous or heterogeneous, solid or liquid, neutral, bipolar, ionic – (positive or negative) as well as symmetric or asymmetric.(Matsuura, 1993; NATH, 2008)

Symmetric membranes generally have a uniform structure throughout the entire membrane thickness. Due to this uniformity, the transport properties are identical and easily determined from the overall structure of the membrane. The symmetric membranes applications include dialysis and electro-dialysis. In contrast, the structure of asymmetric membranes is not uniform and they usually have a gradient in the structure; the structural and transport properties are also not uniform across the membrane thickness.(Buonomenn, 2011) The asymmetric membrane is usually composed of two distinct layers; a very thin skin layer and a more porous, thick substructure which serves as a mechanical support for the skin layer. The skin layer is usually facing the high pressure side and the transport properties are determined by the properties of this layer.

Some of the important transport properties used in the description of flow through porous media and characterization of the structure include the porosity, permeability, and tortuosity. (Duda, Koza, & Matyka, 2011; Matyka, Khalili, & Koza, 2008) Although, there is a wide variety of definition of tortuosity available in the literature, it is generally agreed that tortuosity attempts to describe the convolution in porous media – convolution present as a result of not parallel and not completely straight streamlines. Several approaches have been employed in estimating the tortuosity in asymmetric porous media. This has led to the emergence of various types of tortuosity – hydraulic tortuosity, diffusive tortuosity(Cornell & Katz, 1953), electric tortuosity and acoustic tortuosity(Johnson, Plona, Scala, Pasierb, & Kojima, 1982), streamline tortuosity as well as geometric tortuosity. (Matyka et al., 2008)

3.2 PROBLEM DEFINITION

In Room Temperature Ionic Liquid (RTIL) membranes, Dr Scovazzo noted that the overall mass transport may depend largely on the porous support morphology.(Scovazzo, 2010) For separation processes using liquid membranes, the rate of separation depends on the effective diffusion tortuosity of the porous support. However, the fluid flow tortuosity is generally used in the analysis. It has been noted that diffusion tortuosity bears little semblance to fluid flow tortuosity and it can sometimes be 10 times larger than the fluid flow determined value.(Cussler, 1997) A model was developed to explain a similar phenomenon in porous aquifers.

This chapter continues the exploration of RTIL membranes and is in furtherance of the RTIL research being carried out in Dr Scovazzo's lab. It explores the work done by Dr Holt in developing a model to explain similar behavior in porous aquifers.(Holt, 1997)

The following lays a foundation, starting with the fundamentals of porous media transport; the one-dimension diffusive resistance to mass transport in porous media, R is

$$R = \frac{1}{D_e}\frac{L}{A} \tag{3.1}$$

Where D_e is the effective diffusivity, L = thickness of porous medium, and A = area perpendicular to the direction of diffusive mass transport. If τ, tortuosity, is defined as the effective transport length by the thickness (L_e/L), and ϕ is the volumetric porosity i.e. pore volume divided by the total volume; this results in the typical form of effective diffusivity reported in the literature

$$D_e = D\frac{\phi}{\tau} \tag{3.2}$$

Equation (3.2) is for a porous medium with a uniform areal porosity and does not apply to asymmetric porous media. A more general form of equation (1) was proposed by Holt

$$R_p = \frac{1}{D}\int_0^L \frac{\tau}{A_p(x)}dx \tag{3.3}$$

Where D = bulk fluid diffusivity, $A_p(x)$ is the flux direction dependent cross-sectional area of the pores perpendicular to the direction of diffusive mass transport and τ is the tortuosity, assumed to be independent of x. Now defining $\overline{\phi}_A^H$ as the harmonic mean of the areal porosity (A_p/A) along the direction x. The effective diffusivity, in this harmonic mean model then becomes

$$D_e = D\frac{\overline{\phi}_A^H}{\tau} \tag{3.4}$$

Now there are two forms of effective diffusivity; the general form of Eq (3.4) and the uniform areal porosity form of Eq (3.2). In practice, however Eq (2) typically yields unrealistically high estimates of tortuosity, as Eq (3.2) does not consider the effects of pore space heterogeneity. In contrast the variability of $\overline{\phi}_A^H$ in Eq (3.4) alone is sufficient to account for the order of magnitude reductions in effective diffusivity observed in experiments. This harmonic mean model was tested by fabricating scaled-up models of asymmetric porous membranes with known $\overline{\phi}_A^H$ for measurement of their effective diffusivities. If the harmonic mean model is valid, it will give us a tool with which to design better supports for membranes such as RTIL membranes.

3.3 LITERATURE REVIEW

3.3.1 History of Membrane and Membrane Applications

A membrane is usually a thin polymeric solid that controls the permeation of species in contact with it. It can either be homogeneous in which case, it has a uniform composition and structure or heterogeneous which has a non-uniform composition and a non-uniform structure.(Baker, 2012) As early as 1748, Abbé Nolet coined the word osmosis to describe permeation through a diaphragm even though the industrial or commercial applications were not to be developed until much later in the 1960s. Membrane performance is usually determined by the flux - amount of fluid passing through the membrane per unit area of membrane per unit time; and selectivity - which is the fraction of solute in the feed retained by the membrane as in solutes, and particulates in liquids and gases.(Scott & Hughes, 1996) For rate based separations, selectivity is the ratio of permeabilities.

Reliability, cost, selectivity and rate of separation were some of the problems with membrane uses earlier on; all these have been resolved in the last 30 years. One of the major breakthroughs for the transformation from laboratory-based uses to industrial-uses was the discovery of the Loeb-Sourirajan process for making defect-free, high flux, anisotropic reverse osmosis membranes. The membranes from the Loeb-Sourirajan process essentially consist of an ultrathin, selective surface film on a much thicker but much more permeable micro-porous support which provides the mechanical strength.(Baker, 2012)

Currently, membranes have found uses in a wide variety of applications and across different industries. They are used in commercial quantities for the production of potable water from sea water; for recovery of valuable constituents from industrial effluents; for the fractionation of macromolecular mixtures in the food and drug industries and for separation of gases and vapors in petrochemical processes. There have also been increased uses of membranes in biological applications; such as in, artificial organs and drug delivery devices.(Strathmann, Giorno, & Drioli, 2006) Though the research into greater effectiveness and efficiency is still on-going, membrane processes are now the primary separation technology used in waste water reclamation and desalination.

3.3.2 Liquid Membranes

If membranes can be described as semi-permeable phase separators, then the earlier description as thin polymeric solid can be modified to include liquids. Indeed, membranes are now more accurately described as semi-permeable phase separators. The most important feature in liquid membranes is that, while it acts as a separation barrier between two phases or mediums, the transport occurs by the solution-diffusion mechanism.(NATH, 2008) Compared to polymers, liquids have larger diffusion coefficients, and for certain gases, they are also known to have enormous solubility.(Morgan, Ferguson, & Scovazzo, 2005). Due to the lack of porous support by the liquid film, liquids used as membrane are generally stabilized to prevent rupture during storage.

Liquid membranes are generally classified into two types; Non-supported and Supported liquid membranes (SLM). The non-supported liquid membrane is further sub-divided into bulk and emulsion liquid membranes, and supported liquid membranes are further divided into flat sheet liquid and hollow fiber liquid membrane. In an SLM, the membrane phase is immobilized

in the pores of a porous polymer.(Parhi, 2013) The polymeric support only provides a structural support for the membrane phase but does not play an active role in separation. The long term performance and stability of SLMs are still subjects of active research. Usually, the stability of the immobilized membrane is sometimes affected at high temperatures by solvent depletion through evaporation or due to adverse operating conditions (e.g. the transmembrane pressure should not be higher than the breakthrough pressure so that the solvent is not expelled from the membrane pores).(Neves, Crespo, & Coelhoso, 2010) An interesting strategy for improving the stability is the use of Room Temperature Ionic Liquids as the immobilized phased within the pores, due to their negligible vapor pressure.

3.3.3 Room Temperature Ionic Liquids

Room Temperature Ionic liquids (RTILs) are organic salts that remain liquid at or below 150^0C. Essentially, they are thermally stable, non-flammable and have a very low vapor pressure; characteristics that have made them the solvent of choice for most separation processes as solvent losses are greatly minimized. Ionic liquids are known to have a high degree of asymmetry that allows for screening of charges, frustrates packing and thereby inhibiting crystallization.(Morgan et al., 2005)

They largely consist of a bulky cation and an inorganic anion. The cations, anions can be readily modified to change their physical and chemical properties. The potential choices of anion and cation that will result in the formation of RTILs are copious. Just like any good organic solvent, they are able to dissolve polar and nonpolar species.(Baltus, Culbertson, Dai, Luo, & Depaoli, 2004; Brennecke & Maginn, 2001; Lozano et al., 2011; Morgan et al., 2005; Neves et al., 2010; Zhao, Dong, & Zhang, 2012) Some typical examples of well-known different classes of ionic liquids are shown in Figure 3.1. The anion (X^-) of the RTIL can be any of a variety of species:

including nitrate [NO_3^-], acetate [$CH_3CO_2^-$], trifluoroacetate [$CF_3CO_2^-$], tetrafluoroborate [BF_4^-], triflate [$CF_3SO_3^-$], hexafluorophosphate [PF_6^-], and bis(trifluoromethylsulfonyl) imide [$(CF_3SO_2)_2N^-$].

Indeed, there has been an upsurge in RTILs research due to the large solubility of CO_2 in selected ILs. Of all the possible choices of RTILs available, RTILs based on the imidazolium cations have shown the greatest solubility for CO_2, which has been shown to also increase depending on the choice of anion and the length of the alkyl chain.(Baltus et al., 2005; Cadena et al., 2004; Carvalho et al., 2009)

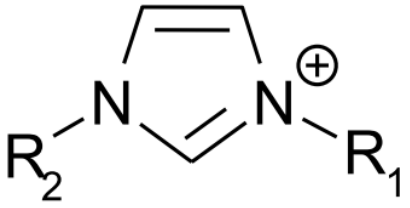

(a) Immidazolium

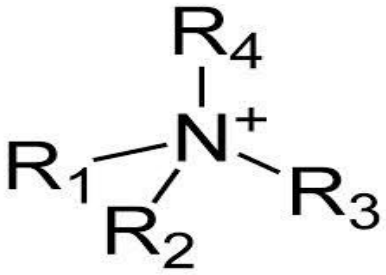

(b) Quaternary ammonium

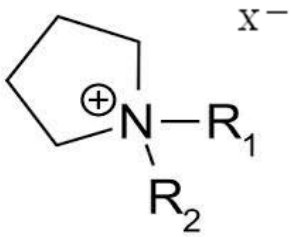

(c) Pyrrolidinium

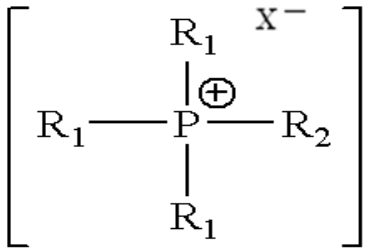

(d) Tetra alkylphosphonium

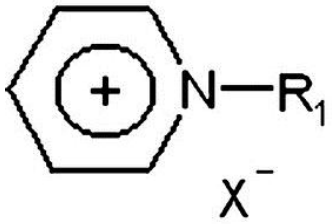

(e) pyridinium

Figure 3.1: Typical examples of well-known different classes of ionic liquids

3.3.4 Gas Permeation: Transport Properties and Fluid Flow

One of the most important models used in the description of the permeation process is the solution-diffusion model. In this model, the permeants dissolve in the membrane material and then diffuse through the membrane down a concentration gradient. This process is described in three main steps; the sorption step, the diffusion through the membrane and the desorption step.(Tremblay, Savard, Vermette, & Paquin, 2006; Wijmans & Baker, 1995) In this model, the transport properties and coefficients of interest are; solubility, and the diffusion coefficient.

The permeability coefficient describes the resistance of fluid flow through a porous material. It is calculated as the product of the solubility coefficient; which is the quantity of gas sorbed by the membrane, and the diffusion coefficient; which indicates how fast a penetrant is transported through the membrane. The permeability coefficient is given as

$$P=D*S$$

where D is the diffusion coefficient and S is the solubility. The unit of the permeability is Barrer.
1 barrer = 10^{-10} $cm^2 \cdot s^{-1} \cdot cmHg^{-1}$

3.3.4.1 Permeation Models

There are quite a number of methods used in the characterization of mass transport in porous media or membranes. Among these methods, three main approaches are prominent;

The differential method; where the rate of penetration through a membrane is measured directly by using a constant partial pressure difference applied to both sides of the membrane;

The sorption method; which looks at how much of the penetrant has been absorbed cumulatively as a result of pressure increase applied to both sides of the membranes. The sorption method can be used with different membrane shapes provided the geometry is well-defined and;

The integral method; where the cumulative amount of the penetrant across the membrane is determined through the application of quasi-constant pressure difference applied to both sides of the membrane. In the integral approach, the permeation process is divided into two parts; the transient state and the steady state. The transient component is represented by the time difference between the time at which the penetrant enters the membrane and the time rate at which the flow rate of diffusing species into the close volume reaches a steady state of permeation.(Rutherford & Do, 1997)The experiment is usually carried out in a dual chamber known as feed and permeates chambers separated by membranes across which the penetrant passes. A pressure sensor is usually attached to this apparatus to collect the pressure data. This represents a major advantage as the calibration requirements are rather not cumbersome and the sensor is not dependent on the nature of the penetrant.

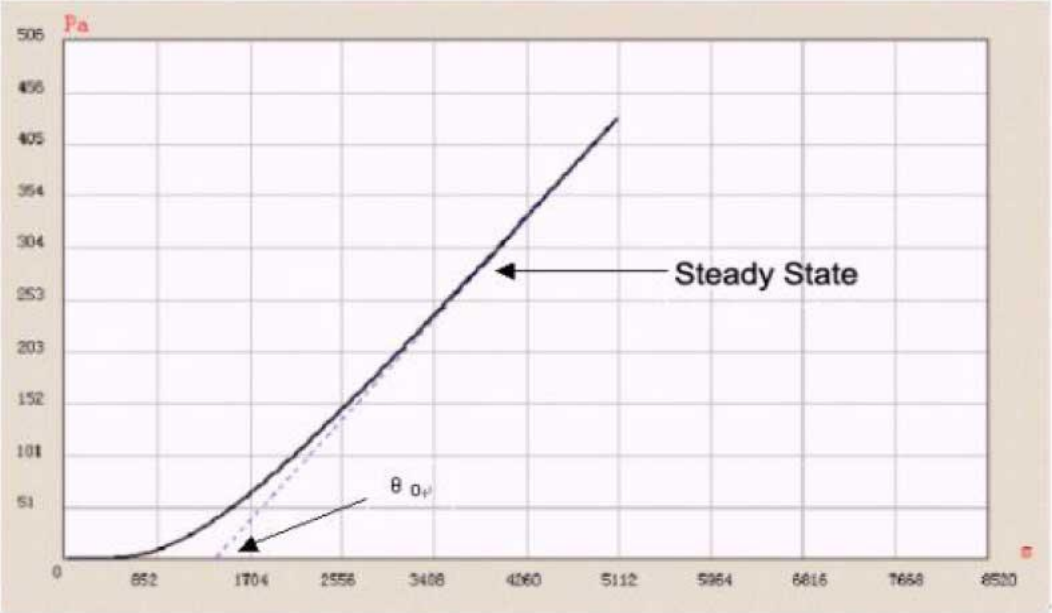

Figure 3.2: A typical permeation figure

These three methods depend largely on the dynamic response obtained from sudden changes in the boundary conditions.(Felder, 1978; Rutherford & Do, 1997; Taveira, Mendes, & Costa, 2003)

Of all the three methods, the integral methods first suggested by Daynes in 1920, particularly offer a very clear and effective technique for determining the transport parameters characterizing the solid-penetrant system. Consequently, this method, also known as the time-lag method has been the method of choice in characterizing the transport parameters in a membrane.(Daynes, 1920)

3.3.5 Tortuosity measurements and effective diffusivity

The measurement of tortuosity and effective diffusivity has been considered by a number of researchers using different and varied techniques both from theoretical examination and experimental analysis.

In 1993, Maskell (Maskell, 1993) proposed that a non-homogeneous membrane has a tortuosity which lies between that of a homogeneous gel and that in a matrix composed of non-conducting particles. He applied this theory to regenerated cellulose. He assumed that the real anionic mobility within the membrane is equal to the anionic mobility in the external solution when a small correction is made for electro-convection.

Li. et al(Li & Dong, 2010) determined the diffusive-tortuosity using a PVT method. The effective diffusion coefficient, D_{eff} and diffusion coefficient, D of CH_4 in a bulk liquid phase were measured in a diffusion cell and the relationship $\varepsilon=D/D_{eff}$ was then used to calculate the diffusive tortuosity.

Also, Croccolo et al.(Croccolo, Bataller, & Pijaudier-cabot, 2010) performed a separation experiment in a thermo-diffusion cell. A temperature difference was applied to a binary mixture while its refractive index was measured by means of a Mach-Zehnder interferometry. They believed that the refractive index showed a fast change due to the thermal gradient and a slower one due to the separation induced by the Soret effect and thus were able to determine the mass diffusion coefficient within the porous medium. The tortuosity values were then calculated using the relation $D^* = D/\tau^2$ where D^* is the molecular diffusion coefficient in the porous medium, D is the molecular diffusion in the free liquid and τ is the tortuosity

More recently in 2014, Manickam et al.(Manickam, Gelb, & McCutcheon, 2014)used X-ray microscopy (XRM) to determine the structural parameter 'S' (function of thickness, tortuosity and porosity of the support layer) of thin film composite (TFC) membrane support layers. The S value was then calculated from the XRM images and was compared to the results obtained from conventional mercury intrusion porosimetery.

3.4 EXPERIMENTAL SECTION

3.4.1 Material Selection Basis

The transport characteristics of RTIL/CO_2 system has been studied by several researchers.(Baltus et al., 2004; Neves et al., 2010) Compared to other RTILs, CO_2 has a higher solubility in imidazolium-based ionic liquids. The presence of acidic hydrogens on the imidazolium ring is believed to be a possible factor for increased CO2 solvation in imidazolium based liquids.(Cadena et al., 2004) CO_2 also reduces the viscosity of [Emim]Tf_2N thereby increasing the diffusivity of CO_2 through it.(Morgan et al., 2005) Additionally, CO2 readily dissolves in [Emim]Tf_2N compared to other anions. Thus making [Emim]Tf2N a more suitable ionic liquid for the experiment.

3.4.2 Materials

The materials used in the study are $C_2F_6LiNO_4S_2$ or Li[Tf2N], LithiumBis(trifluoromethanesulfonyl)imide, 98.0% minimum purity, CAS # 90076-65-6, Lot #2U8VA manufactured by Tokyo Chemical Industry Co., Ltd. $C_6H_{11}BrN_2$ or [Emim]Br; 1-Ethyl-3-methylimidazolium bromide, 98+%, CAS #65039-08-9, Lot # - 10161057 manufactured by Alfa Aesar. Ultrahigh purity CO_2, ON1013, CAS # - (124-38-9), Lot No – 3902011-21-1 was obtained from NexAir (Memphis, TN).

Other material used include porous membranes from Mott® porous media in pore sizes of 0.2A, SO # - 1058693 and 0.5A, Lot # - JJ11542 - 000 and porous Teflon (Pall P/N P5PQ047) were obtained from Pall Corporation.

3.4.3 Apparatus and Procedure

3.4.3.1 [Emim]Tf_2N Synthesis

The synthesis of [Emim]Tf2N from [Emim]Br and LiTf2N is a one to one by mole basis double displacement reaction

$$[Emim]Br + LiTf2N \rightarrow [Emim]Tf2N$$

A known quantity of both chemicals - [Emim]Br, LiTf2N calculated from the amount of [Emim]Tf2N desired was measured. Both chemicals were dissolved in distilled water separately. Thereafter, they were mixed together and poured in a separatory funnel. Furthermore, the solution was shaken vigorously and allowed to sit for a day. After 24 hours, the water was decanted off. Water was added and decanted every 24 hours for 72 hours to extract impurities. Subsequently, the RTIL was placed in the Rotovac overnight at 100^0C and 10 Torr to ensure the water was completely removed from the product.

3.4.3.2 Membrane Saturation

The porous metal membranes were sandwiched together using latex that was trimmed to create a 5 mm rim around membrane and a hydrophobic Teflon porous membrane was placed under the membranes with the shiny surface of the Teflon touching the membrane. The Teflon serves as a backing material to prevent the pressure displacement of the liquid from the pores of the membranes. The porous membranes were saturated with the [Emim]Tf_2N by placing the membranes in the saturation chamber with the hydrophobic membrane facing down. The CO_2 gas was turned on to allow small flow of CO_2 through membrane pores; this forces N_2 and O_2 out of the pores. The ionic liquid was subsequently poured on top of membrane and filled halfway through the top of the saturation device. The CO_2 was turned down to allow only a few bubbles

and was run for approximately 15 minutes. Subsequently, the CO_2 was turned off and the [Emim]Tf_2N was allowed to sit overnight before being placed into the diffusion chamber.

The saturation ensures the [Emim]Tf_2N was immobilized in the membranes. This eliminates free convection and ensures mass transport is limited only to molecular diffusion (a low Rayleigh number). The porous metal membranes were chosen for their hydrophilic nature and thickness which ensured wettability with the ionic liquids and measurable lag times.(Morgan et al., 2005)

3.4.3.3 Diffusion Chamber

After the membranes were saturated with the [Emim]Tf_2N. The diffusivity experiments were carried out in a diffusion chamber. The diffusion chamber is a stainless steel dual chamber cell shown in figure 3.3 on the next page.

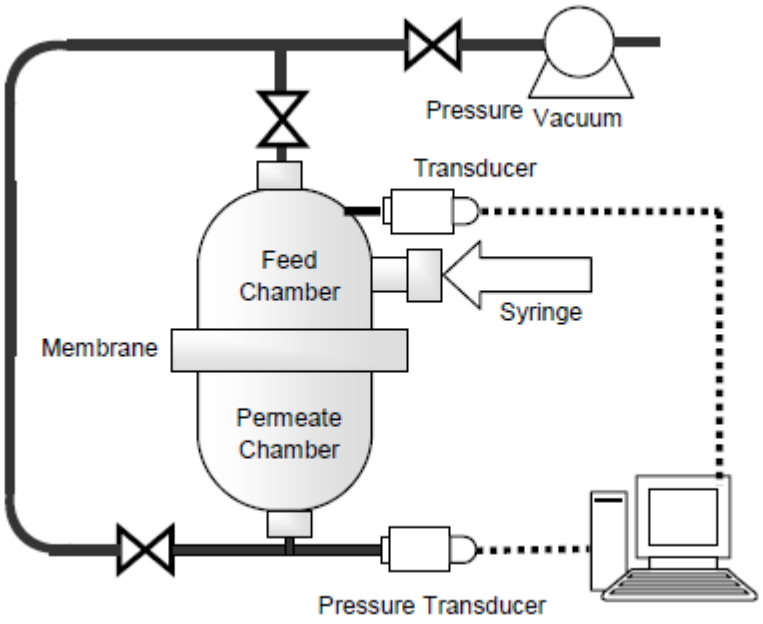

Figure 3.3: Schematic of the Diffusion Chamber. With the cell initially under vacuum, gas is injected into the feed chamber and diffuses through the membrane to the permeate chamber. The flux through the membrane is measured by the pressure rise in the permeate chamber.

The volume of the upper (feed) and lower (permeate) chambers are 90 and 86mL respectively and determined by the pressure due to the containment of a known amount of gas at a fixed temperature. The chamber was shielded from the atmosphere by the compression of two Viton O-rings and was further clamped using a stainless steel clamp. A Fisher Scientific Maxima C plus vacuum pump with a pressure rating of 10^{-4} Torr was used to establish a vacuum in the chamber. The upper chamber had a septum port for the injection of CO_2 gas using a syringe and the gas flux through membrane was measured by monitoring the pressure rise in the permeate chamber with a 0-5 psia (0-34.5 kPa) pressure transducer (Omega PX 811-005 AV). The temperature around the entire unit was regulated using a thermostatic box and a heat source which ensures the temperature of the chamber was kept at 30^0C. The temperature was measured by a temperature sensor.

3.4.3.4 Membrane Placement in Chamber

The membrane was placed in the lower part of the diffusion chamber with the hydrophobic Teflon facing down. The upper chamber was put in place and the system fastened with the chamber clamp. The upper chamber valve was opened, followed by the lower chamber and the main vacuum valve. The vacuum pump was turned on and was allowed to run overnight to ensure the liquid was completely degassed. After the vacuum pump was turned off, 10mL volume of CO_2 was collected using a syringe and allowed to come to equilibrium with the system. Thereafter, the CO_2 was injected into the diffusion chamber through the septum port.

The pressure data was collected for 360 minutes at an interval of 0.1minutes for the first 1 minute and then at an interval of 1 min for the remaining duration.

3.5 METHODS

3.5.1 Lag Time Technique

The data obtained was analyzed using the lag time technique. The method described and the governing boundary conditions have been defined in a previous journal article by Morgan et al. reproduced below.(Morgan et al., 2005) Implicit in this method is the assumption that, the transport through the ionic liquid is primarily by the solution-diffusion mechanism. It is also assumed that there is no boundary layer resistance at the membrane interface. This assumption is valid because diffusion through the liquid membrane is the rate limiting step (by orders of magnitude). With these two conditions, molecular diffusion and no gas boundary layer, the concentration profile in the ionic liquid in the membrane at any time is obtained by Fick's second law of diffusion for a porous medium.

$$\frac{\partial c_i}{\partial t} = \frac{D_i \partial^2 c_i}{\tau^2 \partial z^2} \tag{3.5}$$

where c_i is the concentration of species I, D_i is its diffusivity, and τ is the tortuosity of the medium. A more specific definition of the problem specifies the membrane be initially free of permeating gases. At time zero, the feed chamber is charged with a gas to a pressure P*io*, which will remain constant for all times under consideration. Additionally, the permeate chamber gas concentration will remain negligibly small (i.e., the permeate pressure will remain near zero). These considerations lead to the following boundary conditions:

$$t = 0 \quad 0 \le z \le L \quad c_i = 0$$

$$t > 0 \quad z = 0 \quad c_i = c_{io} = P_{io}S_i \tag{3.6}$$

$$t > 0 \quad z = L \quad c_i = c_{iL} \approx 0$$

where S_i is the solubility of species *i* in the liquid membrane and *L* is the thickness of the membrane. The solution for the concentration profile is readily known and given by

$$\frac{c_{io} - c_i}{c_{io}} = \frac{z}{L} + \frac{2}{\pi}\sum_{n=1}^{\infty}\frac{1}{n}\sin\left(n\pi\frac{z}{L}\right)\exp\left(-n^2\pi^2\frac{D_i t}{L^2\tau^2}\right) \tag{3.7}$$

To find the permeate pressure variation with time, the flux is evaluated at the membrane-permeate chamber interface

$$\frac{V_L}{RT}\frac{dP_{iL}}{dt} = \phi A_{ji} = -\phi A\frac{D_i}{\tau}\left(\frac{dc_i}{dz}\right)_{z=L} \tag{3.8}$$

Where *A* is the nominal membrane area, V_L is the permeate chamber volume, and ϕ is the membrane porosity. Evaluation of Equation (3.4) in combination with Equation (3.3) in the steady-state regime gives an expression for the pressure rise in the permeate chamber with time:

$$P_{iL} = \frac{\phi}{\tau}\frac{D_i ART}{LV_L}P_{io}S_i\left(t - \frac{L^2\tau^2}{6D_i}\right) \tag{3.9}$$

The quantity $L^2\tau^2/6D_i$ is the lag time and this linear expression allows for the determination of both the solubility and diffusivity by computing the slope and abscissa intercept from experimental data.

3.6 RESULTS AND DISCUSSION

The results of the experiment are presented in this section. The experiment was carried out on 2 different membrane configurations – 0.2-0.2μm and 0.5-0.5μm sizes. Three different runs were carried out across of each of these configurations.

For clarity, the results have been presented in the form of tables and graphs. The runs were repeated to show the repeatability of the results and ensure consistency.

The model effective diffusivity was calculated using equation 2.2 which takes into account the variability using the harmonic mean values of the porosity

$$D_e = D * \frac{\overline{\phi}_{\mathrm{A}}^{\mathrm{H}}}{\tau} \tag{3.10}$$

The bulk diffusivity and solubility values of CO_2 in $EmimTf_2N$ are **$0.66*10^{-5}$** (cm^2/s) and 0.09 (mol/L atm) respectively was obtained from literature as reported by Moganty et al. (Moganty, Baltus, & Rt, 2010). and Morgan et al. (Morgan et al., 2005). Both values were used in the determination of the effective diffusivity

The porosity values were calculated using the harmonic mean equation with the individual porosity values as provided by the membrane manufacturers – Matt Corporation. An effective tortuosity value of '2' was used as determined from fundamental principles.

For the determination of the effective diffusivity, the relationship between slope and effective diffusivity was used as given by equation (3.5)

$$Slope = \frac{\phi}{\tau} \frac{D_i ART}{LV_L} P_{io} S_i \tag{3.11}$$

So, the experimental effective diffusivity through the membrane is calculated from;

$$D_{eff} = \frac{slope * L * V_L}{A * R * T * P_i * S_i} \tag{3.12}$$

and the results are presented in Tables 4.1 through Table 4.4 and Figures 4.1 through Figures 4.4. The model results show similar results to the experimental values for both membrane configuration sizes. The model value for the 0.5-0.5μ is a little different but it still has the same order of magnitude as the experimentally determined values.

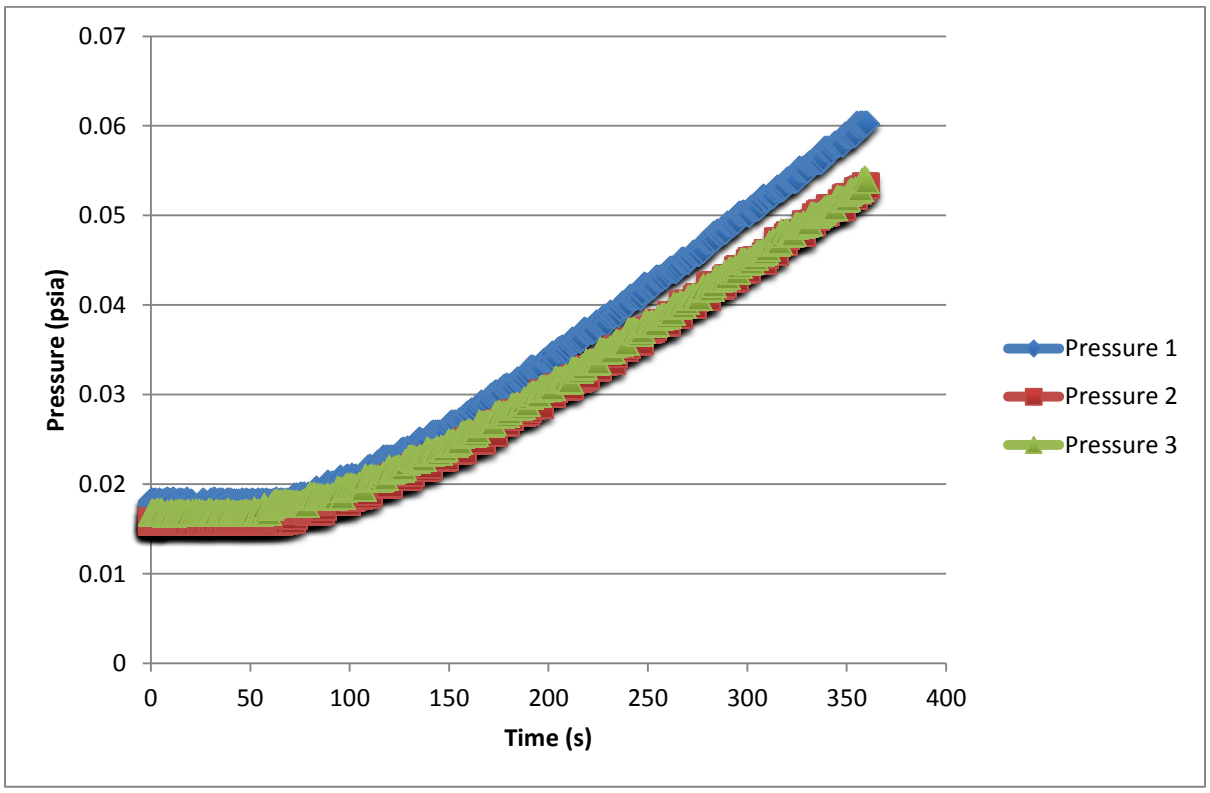

Figure 3 4: Plots of the diffusion cell pressure against time in seconds for the 0.2-0.2µ membrane.

Table 3.1: Pressure versus time for different runs for the 0.2-0.2μ membrane showing a distinct transient and steady-state zone

Injection of:	Carbondioxide	Error	Relative Error
Injection Volume (mL)	5	0.5	0.1
Temperature (K)	254	1	0.003937008
Atmospheric Pressure (psia)	14.7	0.01	0.000680272
Feed Chamber Volume (mL)	98.91		0.6%
Permeate Chamber Volume (mL)	80.5		0.6%
Initial Pressure (psia)	0.743099788		10.02%
	Membrane		
	Area (cm^2)	18.292	0	
	Support Porosity	0.168	0	
	Tortuosity	2	0	
	Thickness (μm)	1981	254	12.82%
Slope (psi/s)		2.35E-06	0.000000008	0.35%
Ordinate Intercept (psi)		-0.01393857	0.000120419	0.86%
Abscissa Intercept (s)		5923.464942		
Correlation Coefficient		0.998778519		

Table 3. 2: Summary results for the 0.2-0.2μ membrane

	Membrane 1 (0.2)	Membrane 2 (0.2)
Porosity	0.168	0.168
Tortuosity	2	2
Length (cm)	0.09906	0.09906
Length/porosity	0.589642857	0.589642857
Harmonic Mean	0.168	
Effective Diffusivity		
Model	5.544E-07	
Experimental	1.925E-07	

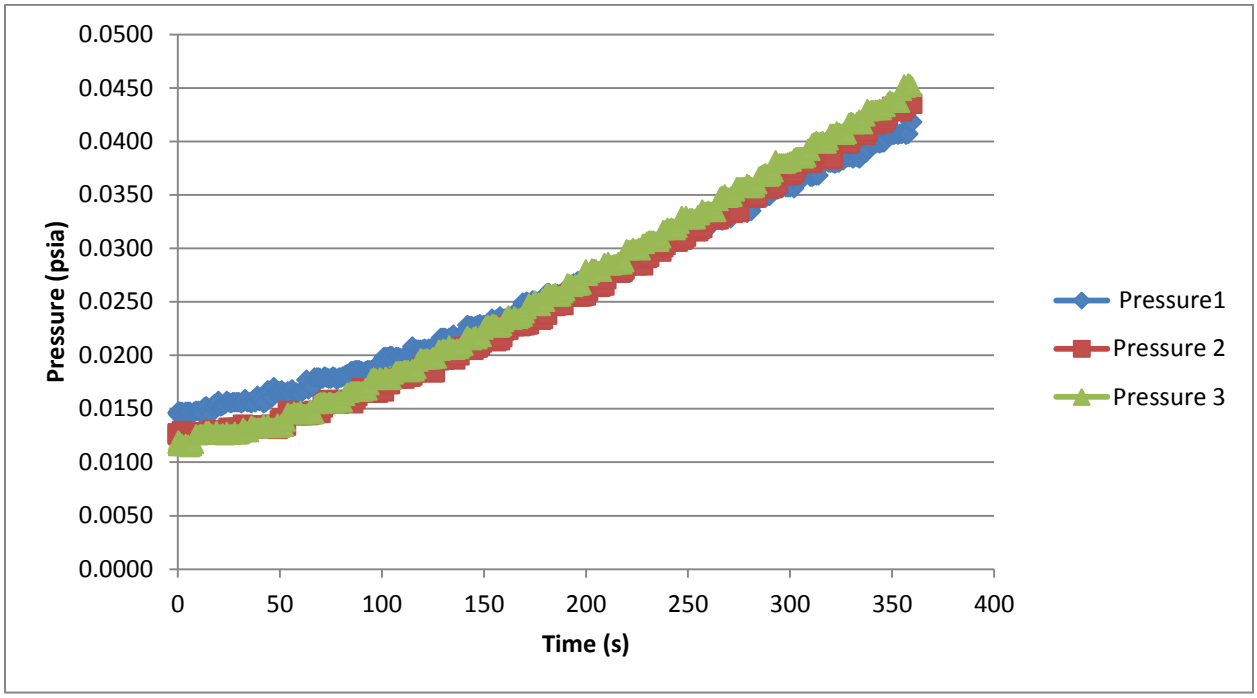

Figure 3.5: Pressure versus time for different runs for the 0.5-0.5µ membrane showing a distinct and well- formed transient and steady-state zone.

Table 3.3: Summary of the calculations for the 0.5-0.5μ membrane

		Error	Relative Error
Injection Volume (mL)	5	0.5	0.1
Temperature (K)	254	1	0.003937008
Atmospheric Pressure (psia)	14.7	0.01	0.000680272
Feed Chamber Volume (mL)	98.91		0.6%
Permeate Chamber Volume (mL)	80.5		0.6%
Initial Pressure (psia)	0.743099788		10.02%
	Membrane		
	Area (cm^2)	18.292	0	
	Support Porosity	0.068	0	
	Tortuosity	2	0	
	Thickness (μm)	2387.6	10	0.42%
Slope (psi/s)	0.00000181	0.000000047	2.59%
Ordinate Intercept (psi)	-0.00848985	0.000834006	9.82%
Abscissa Intercept (s)	4687.587549		
Correlation Coefficient	0.974834775		

Table 3.4: Summary results for the 0.5-0.5μ membrane

	Membrane (1) (0.5)	Membrane (2) (0.5)
Porosity	0.257	0.257
Tortuosity	2	2
Length (cm)	0.11938	0.11938
Length/porosity	0.464513619	0.464513619
Harmonic Mean	0.257	
Effective Diffusivity (cm^2/s)		
Model	8.481E-07	
Experimental	8.480E-07	

LIST OF REFERENCES

3.7 REFERENCES

Baker, R. W. (2012). *Membrane Technology and Applications (Google eBook)* (p. 592). John Wiley & Sons. Retrieved from http://books.google.com/books?id=FhtBKUq4rL8C&pgis=1

Baltus, R. E., Counce, R. M., Culbertson, B. H., Luo, H., DePaoli, D. W., Dai, S., & Duckworth, D. C. (2005). Examination of the Potential of Ionic Liquids for Gas Separations. *Separation Science and Technology*, *40*(1-3), 525–541. doi:10.1081/SS-200042513

Baltus, R. E., Culbertson, B. H., Dai, S., Luo, H., & Depaoli, D. W. (2004). Low-Pressure Solubility of Carbon Dioxide in Room-Temperature Ionic Liquids Measured with a Quartz Crystal Microbalance, 721–727.

Bear, J., & Bachmat, Y. (1990). *Introduction to Modeling of Transport Phenomena in Porous Media* (p. 553). Springer. Retrieved from http://books.google.com/books?id=MOaoeI9aAc0C&pgis=1

Brennecke, J. F., & Maginn, E. J. (2001). Ionic liquids: Innovative fluids for chemical processing. *AIChE Journal*, *47*(11), 2384–2389. doi:10.1002/aic.690471102

Buonomenn, A. G. M. G. (2011). *Membrane Technologies and Applications*. (P. Kaustubha, Mohanty; Mihir, Ed.) (p. 522). Boca Raton: CRC Press. Retrieved from http://books.google.com/books?id=JoTkt7rU2VAC&pgis=1

Cadena, C., Anthony, J. L., Shah, J. K., Morrow, T. I., Brennecke, J. F., & Maginn, E. J. (2004). Why Is CO 2 So Soluble in Imidazolium-Based Ionic Liquids ?, (13), 5300–5308.

Carvalho, P. J., Álvarez, V. H., Machado, J. J. B., Pauly, J., Daridon, J.-L., Marrucho, I. M., … Coutinho, J. a. P. (2009). High pressure phase behavior of carbon dioxide in 1-alkyl-3-methylimidazolium bis(trifluoromethylsulfonyl)imide ionic liquids. *The Journal of Supercritical Fluids*, *48*(2), 99–107. doi:10.1016/j.supflu.2008.10.012

Corey, A. T. (1994). *Mechanics of Immiscible Fluids in Porous Media* (p. 252). Water Resources Publication. Retrieved from http://books.google.com/books/about/Mechanics_of_Immiscible_Fluids_in_Porous.html?id=2K8iFk9PsCoC&pgis=1

Cornell, D., & Katz, D. L. (1953). Flow of Gases through Consolidated Porous Media. *Industrial & Engineering Chemistry*, *45*(10), 2145–2152. doi:10.1021/ie50526a021

Coutelieris, F. A., & Delgado, J. M. P. Q. (2012). *Transport Processes in Porous Media* (p. 236). Springer. Retrieved from http://books.google.com/books?id=vrgPWCDT6LcC&pgis=1

Croccolo, F., Bataller, H., & Pijaudier-cabot, G. (2010). Determination of the Tortuosity of a Porous Medium by Means of A Thermodiffusion Cell, 287–293.

Cussler, E. L. (1997). *Diffusion: Mass Transfer in Fluid Systems* (p. 580). Cambridge University Press. Retrieved from http://books.google.com/books/about/Diffusion.html?id=TGRmfTrsPTQC&pgis=1

Darby, R. (2001). *Chemical Engineering Fluid Mechanics*. *Vasa*. Basel, Switzerland: Eastern Hemisphere Distribution. Retrieved from http://medcontent.metapress.com/index/A65RM03P4874243N.pdf

Daynes, H. a. (1920). The Process of Diffusion through a Rubber Membrane. *Proceedings of the Royal Society A: Mathematical, Physical and Engineering Sciences*, *97*(685), 286–307. doi:10.1098/rspa.1920.0034

Duda, A., Koza, Z., & Matyka, M. (2011). Hydraulic tortuosity in arbitrary porous media flow.

Felder, R. M. (1978). Estimation of gas transport coefficients from differential permeation, integral permeation, and sorption rate data. *Journal of Membrane Science*, *3*(1), 15–27. doi:10.1016/S0376-7388(00)80408-1

Holt, R. M. (1997). Conceptual Model for Transport Processes in the Culebra Dolomite Member , Rustler Formation Sandia National Laboratories, (August).

Johnson, D., Plona, T., Scala, C., Pasierb, F., & Kojima, H. (1982). Tortuosity and Acoustic Slow Waves. *Physical Review Letters*, *49*(25), 1840–1844. doi:10.1103/PhysRevLett.49.1840

Li, Z., & Dong, M. (2010). Experimental Study of Diffusive Tortuosity of Liquid-Saturated Consolidated, 6231–6237.

Lozano, L. J., Godínez, C., de los Ríos, A. P., Hernández-Fernández, F. J., Sánchez-Segado, S., & Alguacil, F. J. (2011). Recent advances in supported ionic liquid membrane technology. *Journal of Membrane Science*, *376*(1-2), 1–14. doi:10.1016/j.memsci.2011.03.036

Manickam, S. S., Gelb, J., & McCutcheon, J. R. (2014). Pore structure characterization of asymmetric membranes: Non-destructive characterization of porosity and tortuosity. *Journal of Membrane Science*, *454*, 549–554. doi:10.1016/j.memsci.2013.11.044

Maskell, W. C. (1993). Tortuosity Factor in Non-Homogeneous Membranes. *Berichte Der Bunsengesellschaft Für Physikalische Chemie*, *97*(5), 680–683. doi:10.1002/bbpc.19930970507

Matsuura, T. (1993). *Synthetic Membranes and Membrane Separation Processes* (p. 480). CRC Press. Retrieved from http://books.google.com/books?id=LHHGLy4eulgC&pgis=1

Matyka, M., Khalili, A., & Koza, Z. (2008). Tortuosity-porosity relation in porous media flow. *Physical Review. E, Statistical, Nonlinear, and Soft Matter Physics*, *78*(2 Pt 2), 026306.

Moganty, S. S., Baltus, R. E., & Rt, V. I. L. F. I. L. (2010). Diffusivity of Carbon Dioxide in Room-Temperature Ionic Liquids, 9370–9376.

Morgan, D., Ferguson, L., & Scovazzo, P. (2005). Diffusivities of Gases in Room-Temperature Ionic Liquids: Data and Correlations Obtained Using a Lag-Time Technique. *Industrial & Engineering Chemistry Research*, *44*(13), 4815–4823. doi:10.1021/ie048825v

NATH, K. (2008). *MEMBRANE SEPARATION PROCESSES (Google eBook)* (p. 336). PHI Learning Pvt. Ltd. Retrieved from http://books.google.com/books?id=7tlTmir7h7AC&pgis=1

Neves, L. a., Crespo, J. G., & Coelhoso, I. M. (2010). Gas permeation studies in supported ionic liquid membranes. *Journal of Membrane Science*, *357*(1-2), 160–170. doi:10.1016/j.memsci.2010.04.016

Parhi, P. K. (2013). Supported Liquid Membrane Principle and Its Practices: A Short Review. *Journal of Chemistry*, *2013*, 1–11. doi:10.1155/2013/618236

Rutherford, S. W., & Do, D. D. (1997). Review of time lag permeation technique as a method for characterisation of porous media and membranes. *Adsorption*, *3*(4), 283–312. doi:10.1007/BF01653631

Scott, K., & Hughes, R. (1996). *Industrial Membrane Separation Technology* (p. 305). Springer. Retrieved from http://books.google.com/books?id=tCcYVd-0rOIC&pgis=1

Scovazzo, P. (2010). Testing and evaluation of room temperature ionic liquid (RTIL) membranes for gas dehumidification. *Journal of Membrane Science*, *355*(1-2), 7–17. doi:10.1016/j.memsci.2010.02.067

Strathmann, H., Giorno, L., & Drioli, E. (2006). An Introduction to Membrane.

Taveira, P., Mendes, A., & Costa, C. (2003). On the determination of diffusivity and sorption coefficients using different time-lag models. *Journal of Membrane Science*, *221*(1-2), 123–133. doi:10.1016/S0376-7388(03)00252-7

Tremblay, P., Savard, M., Vermette, J., & Paquin, R. (2006). Gas permeability, diffusivity and solubility of nitrogen, helium, methane, carbon dioxide and formaldehyde in dense polymeric membranes using a new on-line permeation apparatus. *Journal of Membrane Science*, *282*(1-2), 245–256. doi:10.1016/j.memsci.2006.05.030

Wijmans, J. G., & Baker, R. W. (1995). The solution-diffusion model: a review. *Journal of Membrane Science*, *107*(1-2), 1–21. doi:10.1016/0376-7388(95)00102-I

Zhao, Z., Dong, H., & Zhang, X. (2012). The Research Progress of CO2 Capture with Ionic Liquids. *Chinese Journal of Chemical Engineering*, *20*(1), 120–129. doi:10.1016/S1004-9541(12)6037

CHAPTER 4

CONCLUSION

4.1 SUMMARY AND DISCUSSION

Through the use of modified invasion percolation (MIP) and the diffusion equation, we modeled the effect of capillary heterogeneity, viscous force and buoyancy forces on a CO_2 plume diffusing in a heterogeneous medium. The average mass transfer coefficient and average fractional mass of CO_2 left in the domain were determined over a specified time period under different heterogeneous soil structure. The essence is to gain a deeper insight into the controlling mechanism of injected CO_2 transport in the subsurface. This will further help in implementing more effective development, control and monitoring schemes of CO_2 migration in a borehole.

It was observed that the mass transfer coefficient could be easily predicted from the surface area data with a reasonable degree of accuracy and mass transfer coefficient does not depend on saturation in the absence of buoyancy forces as much as it does on the combination of both capillary forces and buoyancy forces. The implication of this is that, for CO_2 sequestration purposes, the dominant factor controlling mass transfer or diffusion is the interplay of the capillary heterogeneity and buoyancy forces; thereby necessitating a thorough understanding of the geology of the soil before sequestration.

For future work, since we modeled the wetting phase as stationary, the impact of flowing water can be modeled to understand the effects, if any; that could add to the rate of mass transfer. Also, the impact of viscous forces can be looked into, though it might be more computationally intensive, it may however provide useful insight into the controlling mechanism of CO_2 diffusion in the subsurface

The diffusion experiment also shows that the harmonic mean model reasonably predicts the effective diffusivity of $CO_{2.}$. As seen from the tables in chapter 3, the effective diffusivity values obtained for the 0.5-0.5μm using the model agrees well with the literature value. The 0.2-0.2μ model has a slight variation but still has the same order of magnitude for the effective diffusivity values compared to existing values in the literature.

In the future, more membrane configurations can be examined to further ascertain the limits of the model. Also further studies can be done using different gases and different RTILs to explore the relationship inherent in these transport properties. Another system configuration using resistivity to measure the effective diffusivity of the membranes with a known separation distance can be designed for improved accuracy. This way the separation distance can be accounted for prior to taking the readings.

LIST OF APPENDICES

APPENDIX A

The appendix for this paper is not attached. This is a copy of the program codes, user manual and all program files used in Chapter 2 of this thesis.

VITA

Name: Oluseye B. Adeyemi

Address: Department of Chemical Engineering
134 Anderson Hall,
University, MS 38677

Education: B.Sc Chemical Engineering, Obafemi Awolowo University, 2010